

Revisiting the Unified Model of Active Galactic Nuclei

Hagai Netzer

School of Physics and Astronomy, Tel Aviv University, Tel Aviv 69978, Israel; email: netzer@wise.tau.ac.il

Annu. Rev. Astron. Astrophys. 2015. 53:365–408

First published online as a Review in Advance on June 18, 2015

The *Annual Review of Astronomy and Astrophysics* is online at astro.annualreviews.org

This article's doi:
10.1146/annurev-astro-082214-122302

Copyright © 2015 by Annual Reviews.
All rights reserved

Keywords

active galaxies, unification, black holes, accretion disks, central torus, star formation, AGN surveys, interferometry, mergers

Abstract

This review describes recent developments related to the unified model of active galactic nuclei (AGNs). It focuses on new ideas about the origin and properties of the central obscurer (torus) and the connection to its surroundings. The review does not address radio unification. AGN tori must be clumpy but uncertainties about their properties persist. Today's most promising models involve disk winds of various types and hydrodynamic simulations that link the large-scale galactic disk to the inner accretion flow. Infrared (IR) studies greatly improved our understanding of the spectral energy distribution of AGNs, but they are hindered by various selection effects. X-ray samples are more complete. The dependence of the covering factor of the torus on luminosity is a basic relationship that remains unexplained. There is also much confusion regarding real type-II AGNs, which do not fit into a simple unification scheme. The most impressive recent results are due to IR interferometry, which is not in accord with most torus models, and the accurate mapping of central ionization cones. AGN unification may not apply to merging systems and is possibly restricted to secularly evolving galaxies.

1. THE AGN FAMILY: CLASSIFICATION AND UNIFICATION

1.1. AGN Classification

An active galactic nucleus (AGN) is defined here as a galaxy containing a massive ($> 10^5 M_{\odot}$) accreting black hole (BH) with an Eddington ratio exceeding the (somewhat arbitrary) limit of $L_{\text{AGN}}/L_{\text{Edd}} = 10^{-5}$, where L_{AGN} is the bolometric luminosity and $L_{\text{Edd}} = 1.5 \times 10^{38} M_{\text{BH}}/M_{\odot} \text{ erg s}^{-1}$ is the Eddington luminosity for a solar composition gas. This definition excludes the Milky Way Galaxy but includes a large number of low-ionization nuclear emission-line regions (LINERs) and low-ionization radio galaxies. Most AGNs include several of the following components.

- A subparsec-rotation-dominated accretion flow that is usually referred to as an accretion disk. Optically thick disks can be geometrically thin (thin accretion disk) or thick (slim, or thick, accretion disk). (The terminology here is not very clear and both names are used for systems that are not geometrically thin. In this article I use the term slim disk.) Optically thin accretion disks or flows are occasionally advection dominated. Such structures are referred to as radiatively inefficient accretion flow (RIAF), or advection-dominated accretion flow (ADAF) (Narayan 2005).
- High-density, dust-free gas clouds moving at roughly Keplerian velocities at a luminosity-dependent distance of 0.01–1 pc from the BH (the broad-line region, BLR).
- An axisymmetric dusty structure with luminosity-dependent dimensions of 0.1–10 pc (the central torus).
- Lower-density, lower-velocity ionized gas (narrow-line region, NLR) extending from just outside the torus to hundreds and even thousands of parsecs along the general direction of the opening in the torus (ionization cones). Most of this gas contains dust except for very close in, in a region referred to as the coronal line region.
- A very thin molecular maser disk similar in size to the torus.
- A central radio jet occasionally associated with γ -ray emission.

These components have been discussed extensively in numerous books and review articles (Blandford et al. 1990, Antonucci 1993, Robson 1996, Peterson 1997, Krolik 1998, Osterbrock & Ferland 2006, Ho 2008, Netzer 2013, Heckman & Best 2014), and the reader is referred to these references for more information.

AGN unification proposes that the large diversity of observed AGN properties can be explained by a small number of physical parameters. The old unification scheme (Antonucci 1993, Urry & Padovani 1995, Urry 2003) is a courageous attempt to combine the ever-increasing number of subgroups into a general picture with two parameters: the torus inclination to the line of sight (LOS) and the source luminosity (unification by inclination). This scheme is perhaps the simplest possible way to characterize the known fact that the nuclear continuum and emission-line radiation of AGNs can suffer wavelength-dependent scattering, absorption, and reflection on the way out. These effects can take place in the torus, in the disk of the host galaxy, in stellar and nuclear outflows, and inside the BLR itself. Heckman & Best (2014) suggested that AGNs can be separated into two major groups: radiative-mode AGNs and jet-mode AGNs. Most of the energy output in radiative-mode AGNs is in the form of electromagnetic radiation and is a direct result of matter accretion through a central optically thick accretion disk. This group is referred to in the literature as Seyfert galaxies or quasi-stellar objects (QSOs). About 10% of the sources in this group are radio-loud, showing a highly collimated, relativistic radio jet and, occasionally, a γ -ray jet. Radiative-mode AGNs are efficient accretors with $L_{\text{AGN}}/L_{\text{Edd}} \geq 0.01$. An alternative name, based on the level of ionization of the NLR gas, is high-ionization AGNs (also called high-excitation AGNs). The prime energy output of jet-mode AGNs is bulk kinetic

energy transported in two-sided jets. Their typical Eddington ratio is much smaller and the jets are most likely powered via a RIAF. The members of this group are low-luminosity radio galaxies and LINERs, and an alternative spectroscopic definition is low-ionization AGNs. In the local Universe, the mean BH mass of LINERs is larger than that of radiative-mode AGNs.

This review concerns mostly radiative-mode AGNs, and the reader is referred to Ho (2008) and Heckman & Best (2014) for more information about radio-mode sources. The exceptions are some LINERs with total electromagnetic radiation that equals and even exceeds, the jet kinetic energy. I do not discuss radio-loud, radiative-mode AGNs—which excludes approximately 10% of radiative-mode AGNs—although most of their properties are indistinguishable from those of the radio-quiet sources. In this review I address the following subgroups.

1.1.1. Type-I AGNs. These sources show broad ($1,000\text{--}20,000\text{ km s}^{-1}$) permitted and semiforbidden emission lines and a bright, nonstellar, central point source visible at all wavelengths that are not contaminated by stellar light. Almost all low- to intermediate-luminosity type-I AGNs show strong, high-ionization narrow emission lines, many of which are forbidden lines. Most papers refer to these sources as Seyfert 1 galaxies or QSOs. Narrow emission lines are missing from the spectrum of many high-luminosity type-I AGNs. Many papers distinguish between several subgroups of type-I AGNs such as type 1.5, type 1.8, or type 1.9. This labeling refers to the relative intensity of the broad and narrow components of the Balmer lines; e.g., type 1.9 AGNs have a stronger narrow component. Here I refer to all such objects as type-Ii, where “i” stands for intermediate (in some papers “i” refers to broad Paschen lines). This designation has been a source of much confusion, because some of the spectroscopic characteristics have little to do with the conditions near the BH (e.g., reddening in the host galaxy) and weak broad lines can also be the result of line and continuum variations.

1.1.2. Type-II AGNs. These sources contain strong narrow ($300\text{--}1,000\text{ km s}^{-1}$) near-infrared (NIR)–optical–UV emission lines that are somewhat broader than those observed in emission-line galaxies of similar types. The lines show clear indications of photoionization by a nonstellar source. The strongest lines are [O III] $\lambda 5007$, [N II] $\lambda 6584$, [O II] $\lambda 3727$, [O IV] $\lambda 25.9\text{ }\mu\text{m}$, [Ne V] $\lambda 3426$, C IV $\lambda 1549$, and the hydrogen Balmer and Lyman lines. Like type-I AGNs, type-II AGNs also show a point X-ray source. Advances in mid-infrared (MIR) spectroscopy resulted in attempts to identify type-II AGNs by the equivalent width (EW) of the silicate $9.7\text{ }\mu\text{m}$ absorption feature in their spectrum. Such methods are not in good agreement with optical classification. Type-II AGNs are further divided into two subgroups. The first group contains hidden type-I sources with broad emission lines seen in polarized light. The second group is less accurately defined and is occasionally referred to as real type-II or true type-II AGNs. They show similar width and excitation narrow lines but no detectable broad lines and little X-ray absorption. Their mean luminosity is below the luminosity of the type-II objects with hidden broad lines. In the local Universe, such objects may represent as much as 30% of all type-II objects although estimates of this fraction vary a lot between studies (Panessa & Bassani 2002, Tran 2003, Shi et al. 2010, Brightman & Nandra 2011b, Marinucci et al. 2012, Merloni et al. 2014).

1.1.3. LINERs. LINERs are AGNs characterized by their low-ionization, narrow emission lines from gas that is ionized by a nonstellar source. Typical strong emission lines in this group are [N II] $\lambda 6584$, [N II] $\lambda 6584$, and [S II] $\lambda 6731$, and the Balmer lines. I only address LINERs with $\text{EW}(\text{H}\alpha) \geq 3\text{ }\text{\AA}$ to avoid confusion with gas ionized by post-asymptotic giant branch (AGB) stars (e.g., Cid Fernandes et al. 2011). LINERs can be divided into type-I (broad emission lines) and type-II (only narrow emission lines) LINERs. Some but not all LINERs show point-like

X-ray and UV sources and UV and X-ray variations (Maoz 2007, Hernández-García et al. 2013). Detailed reviews of LINERs are given by Ho (2008) and Heckman & Best (2014).

1.1.4. Lineless AGNs. This subgroup consists of AGNs with extremely weak, sometimes completely undetected emission lines. They present a nonstellar central source and, occasionally, continuum variability. This general group includes two distinct subgroups: low-luminosity sources (e.g., Trump et al. 2009) and very high-luminosity sources (e.g., Shemmer et al. 2010, Meusinger & Balafkan 2014).

Classifying type-I AGNs is relatively easy except for cases in which the BLR is heavily reddened by foreground dust. Identifying and classifying narrow-emission-line AGNs are more challenging, especially when no hard X-ray data are available, partly because pure star-forming (SF) galaxies (also called HII galaxies), which are more numerous than AGNs, also show the same strong narrow emission lines. An efficient way to separate the groups is to make use of diagnostic diagrams (see Baldwin et al. 1981, Veilleux & Osterbrock 1987, Kauffmann et al. 2003, Kewley et al. 2006) that compare various line ratios that differ according to the nature of the ionizing continuum (stellar or nonstellar). The most useful line ratios are $[\text{O III}] \lambda 5007/\text{H}\beta$, $[\text{N II}] \lambda 6584/\text{H}\alpha$, and $[\text{O I}] \lambda 6300/\text{H}\alpha$. Diagnostic diagrams show several well-defined regions: one that includes high-ionization AGNs, one that includes mostly LINERs, and one that is occupied by SF galaxies. The region between the pure SF systems and AGNs is occupied by composite sources, which have intermediate spectral properties.

Most AGNs known to date were found in large surveys, such as the Sloan Digital Sky Survey (SDSS), through spectroscopic observations with relatively large apertures (e.g., 3 arcsec in the SDSS). The host galaxies of most AGNs are SF galaxies (Rosario et al. 2012, 2013). We can estimate the total emitted SF luminosity, L_{SF} , and distinguish AGN-dominated ($L_{\text{AGN}} > L_{\text{SF}}$) from SF-dominated ($L_{\text{SF}} > L_{\text{AGN}}$) systems. For example, in the spectroscopic 3-arcsec SDSS sample, such a comparison shows that many composite sources are SF-dominated galaxies. Difficulties in identifying AGNs in composite sources can affect the census of local type-II AGNs, their luminosity functions, and their mass functions. The census of type-I AGNs is based on other methods and is not subjected to such uncertainties beyond a redshift of approximately 0.1. **Table 1** provides some of these numbers.

1.2. The Observed Signature of a Central Obscurer

A central obscurer in the vicinity of the BH, with a spherical or axisymmetric geometry, results in several characteristic properties that can be recognized by a remote observer.

Table 1 The fraction of strong-emission-line sources, at two redshift intervals, as derived from diagnostic diagrams of SDSS objects from the Data Release 7 of the catalog

Redshift ^a	SF galaxies	LINERs	Type-II AGNs	Composite sources
0.05–0.1	0.755	0.035	0.04	0.17
0.15–0.2	0.605	0.035	0.11	0.25

^aThe total number of sources in the 0.05–0.1 redshift interval is 108,353 and the number in the 0.15–0.2 interval is 17,572. The selection includes all emission-line objects for which the lines that were used for the classification have a signal-to-noise ratio larger than 3. This introduces a large bias against sources at higher redshifts, especially weak-line LINERs (courtesy of D. Rosario).

Abbreviations: AGN, active galactic nucleus; LINER, low-ionization nuclear emission-line region; SDSS, Sloan Digital Sky Survey; SF, star forming.

1.2.1. Optical-UV absorption and reflection. The original unification scheme (Antonucci 1993 and references therein) included a central axisymmetric dusty structure with a column density large enough to completely obscure the central source in some directions. This obscurer is usually referred to as the central torus, a somewhat ambiguous name that is, nevertheless, retained here. The matter distribution of the simplest torus is smooth. More elaborate structures, made of clumps and interclump material, are preferred by today's observations. The gas at the inner radius of the torus is ionized by the central source. Deeper in, the torus contains dusty molecular gas.

It is interesting to study the observational consequences of placing such a simple geometrical structure around the central BH and accretion disk. The first prediction is that the obscuring column depends on inclination to the LOS, where inclination is measured relative to the z axis of the system (the direction perpendicular to the central disk). Small inclinations, close to face-on, allow a clear view of the central source and high inclinations result in large obscuration at UV-optical wavelengths.

The second prediction is based on the fact that electromagnetic radiation reflected off dust grains and free electrons is polarized, with angle and percentage polarization dependent on geometry and wavelength. The seminal work of Antonucci & Miller (1985) is among the first of many papers that show how to detect hidden broad emission lines using spectropolarimetry and how to infer the BLR kinematics and overall geometry from such observations. Later and deeper polarimetry (e.g., Tran 2003) shows a large fraction of type-II AGNs with no hint of polarized broad lines. While other explanations, such as Compton thick obscurers, have been proposed (e.g., Marinucci et al. 2012), it seems that many such objects are unobscured but void of BLR gas, such as the real type-II AGNs (Section 1.1) that show no detectable broad lines even when not obscured.

1.2.2. X-ray absorption reflection and emission. The next unavoidable consequence is column-density-dependent X-ray absorption. The assumption used here is of an isotropically emitting central X-ray source, possibly a hot corona over the central part of the accretion disk. For a Compton-thin torus, with $N_H < 1.25 \times 10^{24} \text{ cm}^{-2}$, the obscuring column density can be measured by modeling the observed spectrum, provided the intrinsic spectral energy distribution (SED) and the gas metallicity are known (for solar metallicity gas, most of the X-ray absorption beyond 0.3 keV is due to metals).

Several X-ray spectral features can help diagnose the torus properties. The first feature is the Compton hump, an excess of radiation at approximately 20 keV due to the down scattering of hard X-ray photons. Almost all type-I AGNs show Compton humps in their spectra (scattering and reflection are used quite loosely in the literature and both terms refer to Compton scattering followed by absorption; see, e.g., Netzer 1993).

The second feature is due to the reflection off electrons in highly ionized gas. Here the reflected radiation is a mirror image of the intrinsic continuum with intensity that, for all practical purposes, depends only on the geometrical covering factor ($f_C = \Omega/4\pi$, where Ω is the solid angle subtended by the torus). This fraction rarely exceeds a few percent.

The third spectral feature is the K_α iron line. This emission feature is a collection of fluorescence (Auger) K_α transitions and recombination of H-like and He-like iron at energies between 6.4 and 7 keV, depending on the specific ion. The lines are broad and of high ionization if originating from the surface of the central accretion disk or they are narrow and occasionally of low ionization if originating from X-ray illumination of the cold gas in the torus. In cases in which the X-ray continuum is unobscured, the EW of the narrow K_α line depends on the number of absorbed $E > 7.1$ keV photons. For a typical X-ray SED and solar metallicity gas, this is estimated to be $\text{EW}(K\alpha) \approx f_C \times N_H / 10^{21} \text{ eV}$, where complications such as multiple scattering have been ignored

(note that N_H is not necessarily the LOS absorbing column; see Section 3.3). For a torus with a covering factor of 0.5 and a column density of 10^{23} cm^{-2} , $\text{EW}(K_\alpha)$ is approximately 50–100 eV. Indeed, many type-I AGNs show narrow K_α lines with this EW (Bianchi et al. 2009, Ricci et al. 2013, and references therein). An even clearer signature of a central torus is the large $\text{EW}(K_\alpha)$ in Compton-thick sources. In this case, much of the K_α line reaches the observer without being absorbed but most of the central continuum radiation is blocked by the torus. The observer can see only the much weaker reflected continuum, which raises the observed EW dramatically. It can reach 1–2 keV.

1.2.3. Ionization cones. The unobscured ionizing radiation of the central source reaches the gas in the galaxy, causing heat and ionization. As a result, various narrow lines are emitted. A torus-like geometry results in two ionization cones (or bicone). Depending on the geometry and inclination to the LOS, one of the cones may not be observed.

1.2.4. The dusty boundary of the broad-line region. The dust sublimation temperature, T_{sub} , is the maximum temperature attained by a dust grain before it evaporates. T_{sub} depends on the size and composition of the dust grain and the local flux. For interstellar medium (ISM)-type graphite grains, the maximum sublimation temperature is $T_{\text{sub}} \simeq 1,800 \text{ K}$ and for silicate grains, $T_{\text{sub}} \simeq 1,400 \text{ K}$. These numbers can be used to derive a mean sublimation radius, $\langle R_{\text{sub}} \rangle$, which is the minimum radius at which a grain of a certain size can survive the local radiation field. Averaging over ISM-type grain sizes, one obtains the following mean sublimation distances for graphite (C) and silicate (Si) grains (e.g., Barvainis 1987):

$$\langle R_{\text{sub,C}} \rangle \simeq 0.5 L_{46}^{1/2} \left[\frac{1,800}{T_{\text{sub}}} \right]^{2.6} f(\theta) \text{ pc}; \quad \langle R_{\text{sub,Si}} \rangle \simeq 1.3 L_{46}^{1/2} \left[\frac{1,500}{T_{\text{sub}}} \right]^{2.6} f(\theta) \text{ pc}, \quad (1)$$

where $L_{46} = L_{\text{AGN}}/10^{46} \text{ erg s}^{-1}$ and $f(\theta)$ is an angle-dependent term that allows for anisotropy of the central source radiation (Netzer & Trakhtenbrot 2014). For an isotropic source $f(\theta) = 1$ and for a thin disk with electron scattering atmosphere, $f(\theta) = [\cos \theta (1 + 2 \cos \theta)/3]^{1/2}$ (Netzer 2013). The above numbers are computed for a mean grain size of $a = 0.05 \text{ } \mu\text{m}$ and the distance depends roughly on a^{-2} .

Dust can compete effectively with the ionization of the gas because of its large-absorption cross sections at all wavelengths longer than approximately $0.02 \text{ } \mu\text{m}$. For highly ionized gas, $N_{\text{dust}}/N_{\text{H}^0} \propto N_{\text{gas}}/N_{\text{H}^0} \propto U_{\text{H}}$, where U_{H} is the ionization parameter defined over the hydrogen Lyman continuum (Netzer 2013). At high levels of ionization, the dust absorbs a larger fraction of the photons capable of ionizing hydrogen and helium. This absorption reduces the size of the ionized part of the cloud and lowers the intensity of most emission lines. Emission-line photons produced far from the surface of an ionized, dusty gas cloud suffer additional attenuation on their way out because of absorption by the dust. This is most noticeable in lines with high optical depth, where the large number of scatterings of the line photons considerably increases the path length. Thus, a clear prediction of the torus scenario is that the high-velocity gas near the BH will be divided into two distinct regions: dust-free gas with strong line emission and dusty gas with weak line emission (Netzer & Laor 1993).

1.2.5. Infrared emission. A clear prediction of any torus model is a broad IR SED with a total luminosity that depends almost entirely on the fraction of the radiation from the central source absorbed by dust in the torus (a combination of optical depth and covering factor). The radiation may be emitted isotropically or anisotropically, depending on the optical depth and exact geometry. The SED is predicted to show several silicate features centered around $9.7 \text{ } \mu\text{m}$ and $18 \text{ } \mu\text{m}$, either

in absorption or emission, depending on the exact geometry and LOS optical depth. The emitted radiation of basically all AGNs varies in time. This variation results in time-dependent incident flux on the inner torus walls and time-dependent NIR and MIR emission by the dust.

1.3. Unification Schemes

Unification scheme usually refers to two different categories: IR-optical-UV-X-ray unification and radio unification. The first category involves a central dusty torus and can explain the major differences between type-I and type-II AGNs with a surprisingly small number of assumptions. It was first suggested in the late 1980s. The second category combines the torus with a relativistic jet observed in approximately 10% of all high-ionization AGNs. The jet is launched in the vicinity of the BH and is aligned with the symmetry axis of the system. Radio unification can be used to make specific predictions about the observed properties of compact and extended radio-loud AGNs. Radio unification is not covered in this review, but the reader is referred to Urry (2003) and Tadhunter (2008) for references on this topic. LINERs were not included in the first unification schemes.

Recent observations of larger samples of AGNs, and more detailed information about specific sources, lead to the conclusion that the old unification scheme requires three major modifications. The first modification relates to the physics and structure of the central obscurer. The second modification realizes that there are real differences between various subgroups, beyond the dependence on luminosity and torus inclination. These differences can be due to the nature of the central powerhouse (e.g., a RIAF instead of high-efficiency accretion flow) and to the fact that some AGNs lack one or more of the main components, e.g., a BLR or a NLR. The third modification relates to BH and galaxy evolution. This review focuses on these modifications.

1.4. The Era of Selection Effects

Understanding the cosmological evolution of supermassive BHs is key to understanding galaxy evolution. This requires reliable luminosity and mass functions that depend on AGN classification. Although large surveys such as SDSS contain hundreds of thousands of AGNs up to $z \sim 7$, this survey, and basically all others, is hindered by various selection effects. Because the topic of this review is AGN unification, I only mention selection effects that can bias AGN classification.

The use of diagnostic diagrams in spectroscopic surveys such as SDSS to obtain complete AGN samples is limited to low redshift. Beyond $z \sim 0.2$, type-II AGNs with weaker emission lines drop from the sample because of poor signal-to-noise ratios and contamination by stellar absorption lines (weak-line LINERs are already missing from such samples at redshifts as small as 0.1). At $z \geq 0.4$, the $H\alpha$ line, which is crucial for the classification, is shifted beyond the observable range. An alternative method to detect luminous type-II AGNs up to $z \sim 0.83$ (Reyes et al. 2008 and references therein) is to search for strong [O III] lines relative to $H\beta$, which is required not to show a broad component. Unfortunately, large IR spectroscopic surveys are not yet available, and alternative diagnostics, based on emission lines at shorter wavelengths, are not as reliable. Broad-emission-line AGNs are detected by their continuum shape and their broad emission lines. At $z \leq 0.1$, the least luminous type-I AGNs drop from such samples because of strong stellar continuum and large-amplitude continuum variations.

Reddening and obscuration are other reasons for losing sources from large samples. At small redshift, type-II AGNs are affected more than type-I AGNs are. IR-selected samples are less prone to reddening but are biased toward sources with a larger covering factor and against sources with large inclination angles (see Section 2). They are also contaminated by emission from SF regions

in the galaxy. MIR photometric surveys, like those based on observations from the *Spitzer* space telescope (Stern et al. 2005), are efficient in differentiating AGNs from nonactive galaxies. However, as will be shown below, the IR-SED is not uniform enough to unambiguously differentiate between AGN types, and type-II classification is most problematic. Host galaxy contamination affects how low-luminosity AGNs are measured over the entire rest-frame range of 0.3–2 μm . Selecting and classifying AGNs by their hard X-ray continuum is arguably the most reliable method at almost all redshifts. The completeness of this method depends on the energy and flux limit of the specific sample, and various sophisticated methods have been developed to allow for such biases. A major difficulty is the detection of highly obscured, large-column-density X-ray sources at high redshift.

A comprehensive comparison of the efficiency of various methods to discover AGNs is given by Merloni & Heinz (2013). According to their study (see their figure 16 and related explanation), the missing fractions of AGNs in various samples depend on the bolometric luminosity and are roughly optical (B-band) samples, from 70% at $L_{\text{AGN}} = 10^{47} \text{ erg s}^{-1}$ to 90% at $L_{\text{AGN}} = 10^{42} \text{ erg s}^{-1}$; MIR (15 μm) samples, from 50% at $L_{\text{AGN}} = 10^{47} \text{ erg s}^{-1}$ to 70% at $L_{\text{AGN}} = 10^{42} \text{ erg s}^{-1}$; and hard X-ray (2–10 keV) samples, from 0% at $L_{\text{AGN}} = 10^{47} \text{ erg s}^{-1}$ to 40% at $L_{\text{AGN}} = 10^{42} \text{ erg s}^{-1}$.

In Sections 2 and 3 I review today’s torus models and torus observations, respectively. I describe additional, smaller-scale and larger-scale obscurers in Section 4, ionization cones in Section 5, and other galactic components connected to the torus in Section 6. In Section 7 I explain why AGN unification may not apply to major mergers. Finally, Section 8 is a short summary of the main points of this review.

2. DISK AND TORUS MODELS

2.1. Central Disks and Central Tori

How large and how massive is the central structure? How is it connected to the BLR and accretion disk on its inner side, and to the ISM of the host galaxy on its outer side? Is it a torus, a disk, or some other shape? Is such a structure typical of all large bulge galaxies or is BH accretion essential to form and maintain it? And most important, how is this structure formed in active galaxies? The global theoretical framework is presented in this section and the observational consequences are presented in Section 3.

The terminology used in this area of research requires some clarification because central disk, central torus, and central accretion disk have been used quite loosely. In this review, inner accretion disk refers to the accretion flow inside the sublimation radius, where the accreted gas is losing angular momentum through molecular, magnetic, or other sources of viscosity. Many AGNs must contain a much larger disk-like structure, 1–100 pc in size, that connects the inner disk to the host galaxy. The inner part of this structure can have a thick geometry, in which case it becomes the inner torus. The entire structure, which can extend beyond the torus, is the central disk or the Q disk (after the Toomre stability parameter Q , see below). The central disk contains a large amount of molecular gas that, given a large-enough column density, undergoes, e.g., SF activity associated with supernovae (SN) explosions and the growth of a nuclear star cluster. Some of these processes result in local effective viscosity that can make this entire structure a large accretion disk, where gas loses its angular momentum and drifts into the center. The angular momentum of the large disk is not necessarily aligned with the angular momentum of the inner disk. There is also no known reason why such a large disk maintains its properties throughout the accretion episode.

2.2. General Models

Two general types of central disks and central tori have been considered. The first type is theoretical models (e.g., Krolik & Begelman 1988, Emmering et al. 1992, Collin & Zahn 1999, Beckert & Duschl 2004, Schartmann et al. 2005, Elitzur & Shlosman 2006, Hönig & Beckert 2007, Krolik 2007, Collin & Zahn 2008, Vollmer et al. 2008, Wada et al. 2009, Schartmann et al. 2010, Wada 2012) that were developed to explore specific aspects such as the formation, stability, shape, and evolution of the central structure. The models attempt to answer two fundamental questions. (a) What is the mechanism that removes angular momentum from galactic infalling gas, thus allowing the feeding of the central BH? (b) What mechanisms maintain a thick gaseous structure for a long period of time? Important processes considered in this context include blob motions along magnetic field lines, colliding magnetic clumps, radiation-pressure-supported dusty clumps, SF-driven turbulence, SN explosions, and AGN and stellar feedback via radiation pressure and winds, among others. Several analytic and semianalytic models have been proposed, but the hydrodynamic simulations seem to provide more realistic ways to model this complex situation. The second type is phenomenological, ad hoc models that make assumptions about the size, composition, and geometry of the torus to explain the observations, mostly the spatially resolved images and the NIR–MIR SED (e.g., Pier & Krolik 1992, Fritz et al. 2006, Nenkova et al. 2008a, Hönig et al. 2010, Stalevski et al. 2012). These types of models neglect the connection between the torus and its surroundings.

A natural way to describe the accretion problem is to start from the inner disk, assumed in most models to be geometrically thin and optically thick, where the local viscosity allows radial drift of material all the way to the innermost stable circular orbit (ISCO). A natural outer boundary of the accretion disk is its self-gravity radius, R_{SG} , which is the location where local gravity exceeds the vertical component of the central BH gravity and the disk becomes unstable ($Q = 1$). This radius is given by

$$R_{SG} \simeq 1,680 M_9^{-2/9} \alpha^{2/9} [L_{AGN}/L_{Edd}]^{4/9} [\eta/0.1]^{-4/9} R_g, \quad (2)$$

where $M_9 = M_{BH}/10^9 M_\odot$; α is the viscosity parameter, which is of the order of 0.01–0.1; η is the mass-to-radiation conversion efficiency, and R_g is, again, the gravitational radius (Laor & Netzer 1989). For a stationary $M_9 = 1$ BH and a thin accretion disk radiating at $L_{AGN}/L_{Edd} \sim 0.1$, $R_{SG} \simeq 0.04$ pc.

In the absence of additional local heating sources, Q drops below unity beyond the self-gravity radius and the disk is fragmented into clouds that move in the same general plane. The gap that is formed prevents the inflow of additional, more distant material to the center. According to some models (Collin & Zahn 1999, 2008; Duschl & Britsch 2006), a marginally stable situation with $Q \sim 1$ can be maintained over a large distance beyond R_{SG} owing to collisions between clouds, SF activity, and SN explosions that produce turbulence and local viscosity. Such processes allow accretion from much larger radii. For very massive BHs, such a marginally unstable disk can extend to approximately 100 pc and beyond. A challenge of models of this type is to combine all these processes into a coherent SF history that will allow researchers to follow the evolution of the nuclear star cluster.

Another comprehensive semianalytic model by Vollmer et al. (2008) considers gas infall from the galaxy, which results in the formation of a clumpy central disk. This leads to the formation of a torus through three phases of evolution: (a) An initial short and massive gas infall leads to the formation of a turbulent and stellar wind-driven $Q \sim 1$ disk. This is followed by energetic SF processes. (b) Once the SN explodes, the intercloud medium is removed, leaving a massive, geometrically thick collisional disk with a decreasing yet still high mass accretion rate. (c) When the

mass accretion rate has significantly decreased, the torus becomes thin and transparent, similar to the circumnuclear disk in the center of the Milky Way (e.g., Alig et al. 2013). Numerical hydrodynamic simulations by Schartmann et al. (2010) follow the final stages of the model, focusing on BH feeding during the second and third phases. Low-velocity stellar winds, during the AGB phase, starting some 50 Myr after the onset of SF, are suggested to contain enough gas to feed a small central BH for a period of approximately 10^8 years. The origin of such winds is a quasi-spherical star cluster with little angular momentum. The winds collide and form a central thin disk, and the gas is accreted onto the BH via an unspecified viscosity mechanism. Such models are currently limited to small, $\text{few} \times 10^7 M_\odot$ BHs.

A gaseous torus cannot retain a large height-to-radius ratio with pure rotation. Star clusters can retain such a shape but the gas between the stars cannot because cloud collision drives the gas to the plane on a few dynamic timescales. Maintaining a thick gaseous structure requires high-velocity turbulent motion, or outflow motion, and seems to work better in a clumpy medium where there are frequent cloud collisions (Beckert & Duschl 2004). Other mechanisms proposed to maintain a thick structure involve UV, optical, and IR radiation pressure (e.g., Hönig & Beckert 2007, Krolik 2007, Czerny & Hryniewicz 2011, Wada 2012); magnetic winds (Emmering et al. 1992, Königl & Kartje 1994, Elitzur & Shlosman 2006); and SF activity in the inflowing gas. UV-optical radiation by the central accretion disk, and locally (inside the torus) emitted IR radiation, can be combined into a plausible scheme that helps solve the scale height problem. Here clumps are pushed in the radial direction by the radiation from the central source in a way that depends on $L_{\text{AGN}}/L_{\text{Edd}}$ (Hönig & Beckert 2007, Wada 2012). The central source heats the dust in the clumps, which in turn emit IR radiation. The local IR flux diffuses outward and is absorbed and reemitted by neighboring clumps, which results in a radiation pressure force that balances or overcomes the z -component of the central source gravity (Krolik 2007). In this scenario, an active AGN is necessary to both produce the toroidal structure and maintain its thick structure.

The disk wind scenario proposed in Emmering et al. (1992) and discussed in numerous other papers (Königl & Kartje 1994, Kartje & Königl 1996, Bottorff et al. 2000, Elitzur & Shlosman 2006, Elitzur & Ho 2009) consists of a continuous large disk that is fed by cold material from the host galaxy. Close to the BH, it develops a magnetocentrifugal wind that supports rising clumps. In this scenario, the torus is merely a region in the wind that happens to provide a toroid-clumpy structure. Clumps inside the sublimation radius are dust-free and can be viewed as BLR clouds. At larger distances, the clumps are dusty and can be viewed as part of the torus. The exact column density of the clumps differs from one model to the next. It may depend on the magnetic field properties, the ratio of the external accretion rate to the mass outflow rate from the disk, and other factors. The clumps most relevant to the observations are those capable of emitting strong lines, with a column density of at least 10^{22} cm^{-2} . As the clumps rise from the disk, their column density drops dramatically and they disappear from view. The mass outflow rate in several wind models is somewhat smaller than the mass accretion rate through the disk.

A recent development is the understanding that dust can survive in the atmosphere of the inner accretion disk at all distances where the disk effective temperature, T_{eff} , is below the sublimation temperature (Czerny & Hryniewicz 2011). Simple estimates show that at a distance of R_{BLR} (the emissivity-weighted radius of the BLR), $T_{\text{eff}} \sim 1,000 \text{ K}$, roughly the dust sublimation temperature. This raises the possibility that, starting from this distance, the local radiation pressure acting on the local grains is effective enough to raise dusty clumps from the disk surface. As the clumps rise, they are no longer shielded from the central radiation field, which is more intense than the local field; they are being pushed in a radial direction and the dust evaporates. This reduces the push in the vertical direction and the clumps fall back onto the surface of the disk. Further away, the grains in the lifted material can survive the central radiation field and they form a clumpy thick structure.

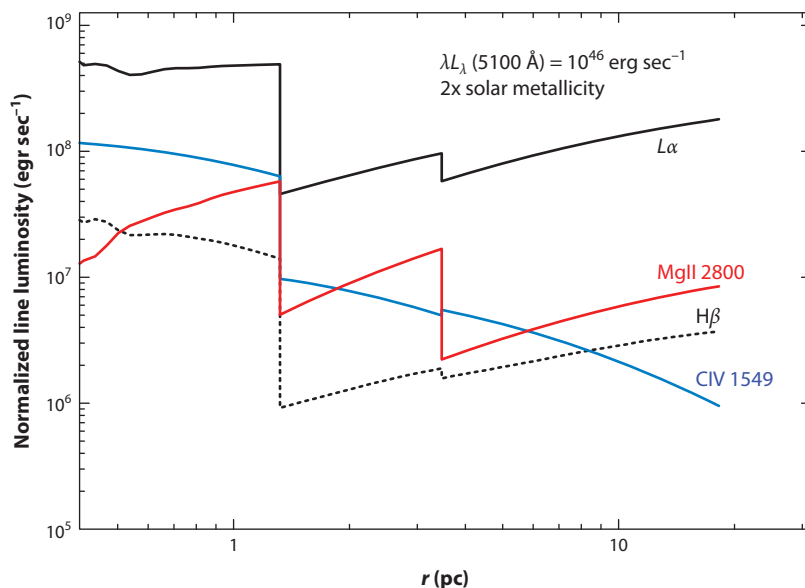


Figure 1

Relative line emissivities per unit covering factor for twice solar metallicity BLR gas as a function of distance from the central BH. For the AGN luminosity considered here ($7 \times 10^{46} \text{ erg s}^{-1}$), the graphite sublimation radius is at 1.32 pc and the silicate sublimation radius is at 3.5 pc. These distances are clearly visible owing to the large drop in the intensity of all lines resulting from the absorption of the ionizing radiation by the grains and to the selective depletion of most metals. Note that some line emission is still present well within the dusty torus (for details of the model, see Mor & Netzer 2012). Abbreviations: AGN, active galactic nucleus; BH, black hole; BLR, broad-line region.

This failed wind scenario is claimed to explain several BLR observations. Its main uncertainties are related to the nature of accretion disks (e.g., thin, thick), the variability of the radiation from the central source, and most importantly, the question of whether the local disk radiation pressure can support very large-column-density dusty clumps.

Disk outflow models, magnetocentrifugal wind, or radiation-pressure-driven wind results in one continuous structure whose geometry is dictated by the global accretion process and whose division into dusty and dust-free regions depends entirely on the central radiation field. A major distinction between the dust-free clouds closer in (BLR clouds) and the dusty clouds farther away is the efficiency of line formation. Line formation can be calculated by photoionization models that provide the predicted emissivity of a specific broad emission line as a function of distance from the central ionizing source. One example is shown in **Figure 1**. The parameters of the dust-free clouds in this model were chosen to reproduce a typical broad-line spectrum with the correct R_{BLR} . The graph shows the dramatic decrease in line emissivity at the graphite and silicate sublimation radii due to the appearance of grains that absorb most of the ionizing flux. The details of the line emissivity depend on the run of ionization parameter, but the global behavior must be typical. Note that line emissivities do not drop to zero and there is additional emission from the dusty part inside the torus.

Perhaps the most realistic models of today are numerical hydrodynamic simulations that include most but not all the processes discussed above. The three-dimensional hydrodynamic simulations of Wada et al. (2009) and Wada (2012) are perhaps the most detailed of their kind. They treat the ISM around a BH with $\sim 10^7 M_{\odot}$ and assume SF and viscosity, which increase during the SN phase.

Wada et al. (2009) consider only stellar feedback and track atomic and molecular hydrogen with a spatial resolution of 0.125 pc. In a quasi-equilibrium state, the gas forms an inhomogeneous disk with a typical diameter of approximately 30 pc. The velocity field of the disk is highly turbulent in the torus region, and the average SN rate is small but large enough to energize the thick structure. The computed gas column densities are consistent with those derived by X-ray observations. A more advanced version of the calculation (Wada 2012) includes AGN radiation pressure (AGN feedback). This drives a fountain, and the interaction between the nonsteady outflow and inflow results in the formation of a geometrically thick turbulent torus. **Figure 2** shows face-on and edge-on views of the density in one such model.

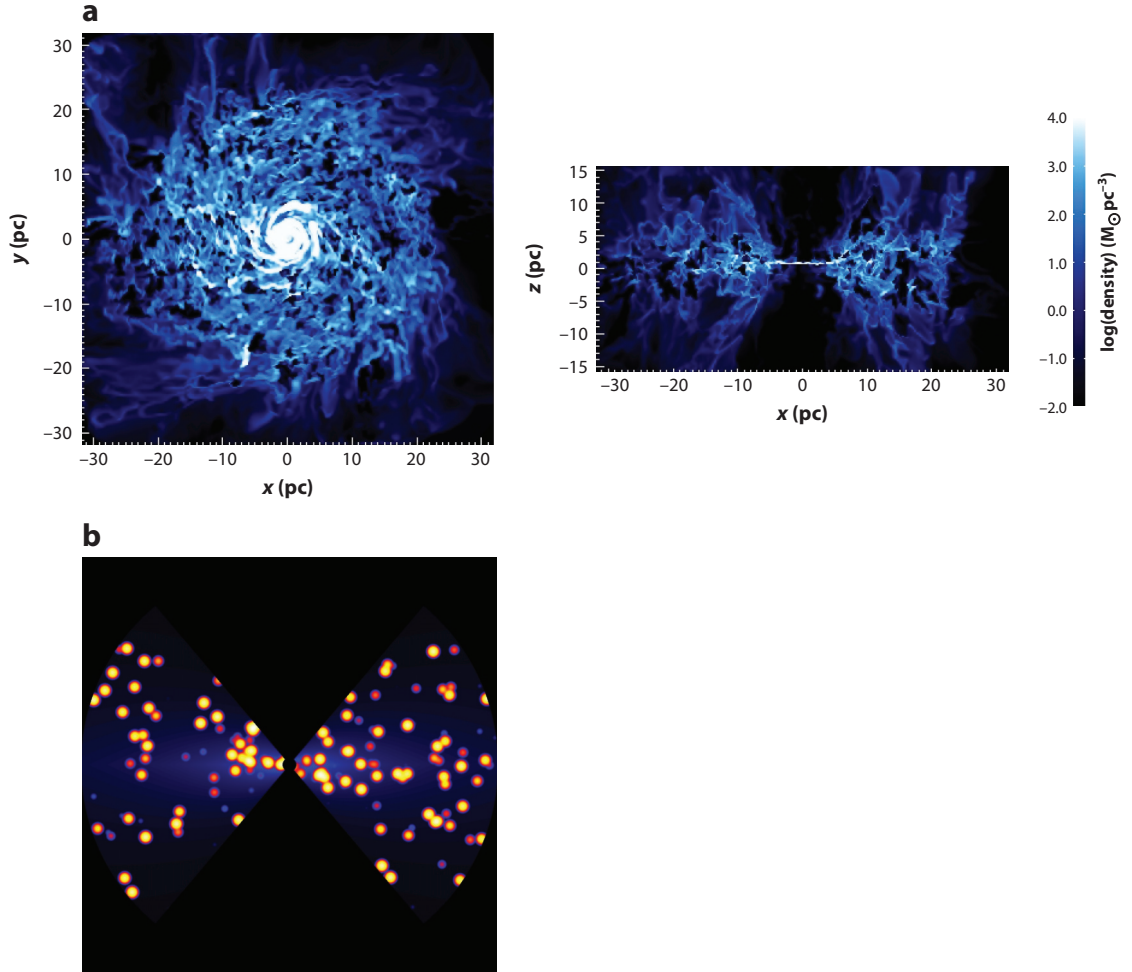


Figure 2

(a) Face-on and edge-on density maps of a central toroidal structure resulting from gas infall toward a 10^7 - M_{\odot} BH in the center of a spiral galaxy as calculated by Wada et al. (2009). Physical processes included in the simulations are SF activity, SN explosions, and stellar feedback (figure courtesy of K. Wada). (b) Edge-on view of the two-phase phenomenological model of Stalevski et al. (2012) showing high-condensation clumps in yellow-orange colors and lower-density interclump dust in blue (figure courtesy of M. Stalevski). Abbreviations: SF, star forming; SN, supernova.

Present-day numerical calculations have limited scope; in particular they treat low-mass BHs and low-accretion-rate systems. It is not at all clear that such scenarios are applicable to AGNs with a BH mass of the order of $10^9 M_\odot$ and accretion rates of the order of $1 M_\odot \text{ year}^{-1}$. At high accretion rates, the local stellar population may be different, the SF events more violent, and the stellar population in the central region different from the one observed in nearby systems.

Two other consequences of all torus models are considered here. The first consequence is the connection between the typical dimensions of the torus and the gravitational potential of the galaxy, which can be quantified by considering the sphere of influence of the central BH. This sphere determines the relative importance of the BH gravity and the bulge gravity for material at the center. It is defined as

$$R_{\text{BH,sph}} = \frac{GM_{\text{BH}}}{\sigma_*^2} \simeq 10.7 \frac{M_{\text{BH}}}{10^8 M_\odot} \left[\frac{\sigma_*}{200 \text{ km s}^{-1}} \right]^{-2} \text{ pc}, \quad (3)$$

where σ_* is the stellar velocity dispersion in the bulge. For $L_{\text{AGN}}/L_{\text{Edd}} = 0.1$, this corresponds to $\text{few} \times 10^6 (\sigma_*/200 \text{ km s}^{-1})^{-2} R_g$. For nearby AGNs, $R_{\text{BH,sph}} \sim 10 \text{ pc}$, similar to and even smaller than the predicted outer dimension of the torus. Thus, the gravitational influence of the stars in the bulge is comparable to that of the central BH and must be included in the calculations.

The second consequence is related to broad-line observations. All the models considered here require continuous flow of gas, from several parsecs to the ISCO. This would block the view of part of the BLR behind the disk in type-I AGNs that are observed close to face-on. The observational implications of this scenario have not been studied so far. The masses in both the torus and the central accretion disk are of the order of 1% of the BH mass, which, given an accretion rate that produces $L_{\text{AGN}}/L_{\text{Edd}} = 0.1$, could supply enough gas for $\text{few} \times 10^6$ years. This raises the possibility that a long accretion episode of approximately 10^8 years is broken into several shorter episodes during which the inner disk is disconnected from the outer flow.

An interesting variant of the general torus formation scenario, proposed by Wang et al. (2010, 2011b), moves the SF activity to inside the dust sublimation radius. This model is not concerned with the issues of torus formation and stability. It merely assumes the existence of a central torus that serves as a source of mass supply to the innermost region. The model includes a thin, central accretion disk around the central BH and fragmented clouds between R_{SG} and the inner walls of the torus. SF activity and SN explosions take place inside the torus walls, and the duration of one accretion episode is estimated to be $\text{few} \times 10^6$ years. This would result in approximately 10^6 stars that may eventually settle into a central star cluster.

2.3. Phenomenological Torus Models

Phenomenological torus models refer to ad hoc models that enable a more accurate treatment of the radiative transfer and better modeling of the emitted SED and the images of the torus at different wavelengths.

2.3.1. Continuous and clumpy tori. Three generic types of phenomenological torus models are continuous (or smooth) gas distribution models (e.g., Pier & Krolik 1992, Efstathiou & Rowan-Robinson 1995, Granato et al. 1997, Dullemond & van Bemmelen 2005, Fritz et al. 2006), clumpy torus models (e.g., Dullemond & van Bemmelen 2005; Nenkova et al. 2008a,b; Hönig et al. 2010), and composite (a combination of clumpy and continuous) models (Stalevski et al. 2012). Feltre et al. (2012) compare the first two types, and Lira et al. (2013) provide a comparison of two clumpy torus models based on fitting the spectra of type-II AGNs.

All phenomenological models are axisymmetric and the torus inner walls are assumed to be at the dust sublimation radius. Unfortunately, the definition of this radius can differ between models because of the different types of grains and the exact method used to estimate the bolometric luminosity of the central sources. Some of the models, e.g., Stalevski et al. (2012), take into account the radiation from an anisotropic central source. This adds an angular term to the torus equations [$f(\theta)$ in Equation 1] to describe the shrinking sublimation radius at large polar angles. In this case, the torus equatorial plane reaches the outer boundary of the central accretion disk. The effect is more noticeable in the case of slim disks, for which the dependence of radiation from the central source on polar angles is more noticeable (Kawaguchi & Mori 2010, 2011; Wang et al. 2014).

The important parameters of the continuous phenomenological models are the inner and outer radii of the torus, the density profile, and the opening angle. Additional parameters of clumpy tori models include the column density of individual clumps, the radial distribution of the clumps (this replaces the run of gas density in the smooth model), the filling factor, and the density distribution of the clumps. Present-day phenomenological models do not yet include different types of grains in different parts of the torus, although this has been considered in simpler (from the point of view of radiative transfer) models (Schartmann et al. 2008).

Radiative transfer is relatively easy to handle in continuous dusty tori but not in clumpy tori. Different studies adopt different approaches to solve this problem. The analytical 1D calculations of Nenkova et al. (2008a) are limited in their ability to treat complicated geometries but can cover a large parameter space with different clump sizes, torus opening angles, and clump distributions. The 3D calculations of Hönig et al. (2010) and Stalevski et al. (2012) are examples of models using a Monte Carlo transfer technique, combined with ray-tracing, which allows for more accurate solutions and, in principle, can deal with different grain sizes and compositions. However, the calculations are computationally intensive and the parameter space explored more limited.

Continuous dust distribution models are characterized by a monotonically decreasing dust temperature as a function of distance from the BH due to the $F \propto r^{-2}$ term and the attenuation of the incident radiation by the dust. In such models, every radius corresponds to a certain temperature. One prediction of continuous models is strong silicate 9.7 μm absorption in cases in which the total optical depth at this wavelength exceeds unity. This is simply the result of material farther away absorbing the flux emitted at this wavelength by the inner torus walls. This effect is predicted to be most noticeable in type-II sources seen at large inclination angles (e.g., Nenkova et al. 2008a).

There are two fundamental reasons why the SEDs of clumpy torus models are different. First, the illuminated and back sides of individual clumps radiate at different temperatures, which allows a certain location in the torus to have a large range of temperatures rather than a single temperature typical of continuous models. Second, and more important, gaps between the clumps allow a free, unattenuated LOS from the center to deep inside the torus. A clump at several R_{sub} can emit at the local, distance-dependent dust temperature, spreading the high-temperature regions over larger parts of the torus. Two important consequences are that the strength of the 9.7 μm absorption feature is much below its predicted strength in continuous distribution cases, and the anisotropy of the emitted radiation is smaller. An obvious limitation is the assumption of empty space between the clouds in a system where cloud collision and evaporation are unavoidable.

Composite models are perhaps the most realistic. In composite models, the volume between clumps is filled with diluted dusty gas, which absorbs part of the incident optical-UV radiation and part of the locally emitted NIR and MIR radiation. The main features of the pure clumpy case are preserved but additional attenuation by the intercloud dust and gas must be taken into account. **Figure 2** shows a schematic structure of the composite torus model of Stalevski et al.

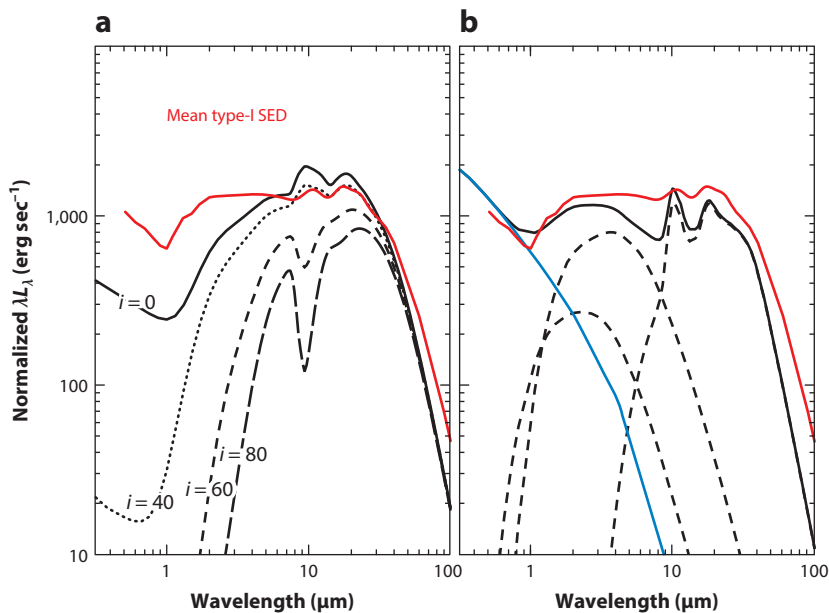


Figure 3

(a) A comparison of the Stalevski et al. (2012) models (*black curves*) and the observed Mor & Netzer (2012) composite type-I SED model (*red line*) that contains dust emission from the NLR (see Section 3). The models are marked with the viewing angle to the torus. (b) The SED of a three-cloud obscurer. The column densities of the clouds are 10^{23} cm^{-2} and the gas-to-dust ratio is galactic. Two of the clouds contain pure graphite grains, are located at the graphite sublimation radius, and are three times farther away. The third cloud contains ISM-type dust and is located 100 times farther away than the first cloud. The covering factors are 0.1, 0.3, and 0.3, respectively. The solid black line is the combination of the three individual SEDs that are marked by dashed lines. The blue line is the SED of the central disk. Abbreviations: ISM, interstellar medium; NLR, narrow-line region; SED, spectral energy distribution.

(2012) and **Figure 3** exhibits several SEDs computed with this model. The SEDs are compared with the composite type-I SED of Mor & Netzer (2012).

To illustrate the difficulty in deriving specific torus properties from comparing models with observations, I show in **Figure 3** a basic model that was constructed by combining the emitted fluxes of three (!) dusty clouds with the same column density, 10^{23} cm^{-2} . The clouds are located at different distances from an accreting BH. Two of them contain pure graphite grains and the third cloud contains graphite and silicate grains similar to what is found in the ISM (see the figure caption for details). This simplest possible theoretical SED is already in reasonable agreement with the observations suggesting that doubling or tripling the number of clouds is all that is required to get a good fit.

Finally, we should note two other types of phenomenological models, the tilted disk model of Lawrence & Elvis (2010) and the combined torus plus dusty polar wind model of Hönig et al. (2013). The first model is discussed in Section 4 and the second in Section 3.

2.3.2. Anisotropy and covering factor. Each of the models discussed above has its own effective covering factor. For smooth torus models, this is simply a matter of geometry and the wavelength-dependent optical depths. For clumpy models, the covering factor depends on the number of clouds and their 3D distribution. In the straw person model of Antonucci (1993), the covering factor is

assumed to be the same for all sources of a given luminosity. The implication for large samples is translated to a simple expression: $f_C = N_{\text{type-II}}/N_{\text{type-I}}$. The realization of a significant spread in f_C at a given luminosity suggests that the covering factor is a second unification parameter (Elitzur 2012). In this case, the relative number of type-I and type-II sources still defines the mean f_C , but a source is more likely to be classified as type-II if its covering factor is larger than the mean and as type-I if it is smaller than the mean. Thus, the high covering factor tail of the f_C distribution contains more type-II AGNs, and the mean covering factor of type-I AGNs is smaller than the mean of type-II AGNs if objects are selected by their optical properties. More quantitatively, if we define the covering factor probability distribution of sources with luminosity L as $P(f_C, L)$, and the probability of a type-I source from this population to have a covering factor f_C , $P_I(f_C, L)$, we can write,

$$P_I(f_C, L) = (1 - f_C)P(f_C, L); \quad P_{II}(f_C, L) = f_C P(f_C, L). \quad (4)$$

Because of the finite probability of seeing the central source at any inclination through a clumpy medium (assuming no dusty interclump material), some sources classified spectroscopically as type-I AGNs have high inclination angles. Similarly, an obscuration by a single large cloud can result in the appearance of a type-II spectrum. This interesting possibility can be tested by observations. For example, the angle of polarization of hidden broad emission lines in face-on tori is predicted to be different from that in edge-on tori. The presence of a lower-density, dusty intercloud medium (Stalevski et al. 2012) changes this simple estimation, but the overall dependence on the angular distribution of the clumps is still an important feature of all clumpy torus models.

Anisotropy is a second characteristic of all torus models. It is most noticeable in continuous gas distribution tori, in which the lowest-distance dust, which is directly heated by the central source, can only be seen from small inclination angles. In clumpy tori, there are always gaps in the distribution and hot clumps can be seen at larger inclination angles. This reduces the anisotropy. Inspection of several models by Stalevski et al. (2012) and Nenkova et al. (2008b) designed to fit observed SEDs suggests that for wavelengths that are optically thick to the torus-emitted radiation, the anisotropy is roughly proportional to $\cos i$, where i is the inclination to the LOS. This is similar to the expected anisotropy of the central accretion disk. At longer wavelengths, where the dust optical depth is smaller, the emission is more isotropic, and at FIR wavelengths the torus emits more like a sphere.

A general, somewhat simplistic approach that does not take into account wavelength dependences is nevertheless useful for improving the estimated geometrical covering factor for type-I AGNs. This approach requires an isotropy parameter b that varies from 1 (complete isotropy) to 0 (maximum anisotropy) and a general dust anisotropy function, $a(b, f_C)$. Assume a case in which the (unknown) covering factor of the torus is f_C and the total AGN bolometric luminosity, L_{AGN} , is completely isotropic and seen, unattenuated, through the opening in the torus; i.e., $(1-f_C)L_{\text{AGN}}$ escapes the system. The total dust emission is $f_C L_{\text{AGN}}$ and the emission through the opening (i.e., the part a remote observer can see) is $L_{\text{dust}} = (1-bf_C)f_C L_{\text{AGN}}$. Recall that flux measurements refer to luminosity per unit solid angle [i.e., divide the AGN and dust emission through the opening by $(1-f_C)$]; we can define an observed ratio, $R = L_{\text{dust}}/L_{\text{AGN}}$, and relate it to the covering factor by requiring $R = a(b, f_C)f_C$, where the anisotropy function is,

$$a = \frac{1 - bf_C}{1 - f_C}. \quad (5)$$

This gives $a(b, f_C) = 1$ for complete isotropy ($b = 1$) and $a(b, f_C) = 1/(1 - f_C)$ for maximum anisotropy ($b = 0$), as required. For example, in a case in which $f_C = 0.7$, complete isotropy of

dust emission gives $R = f_C$, maximum anisotropy gives $R = 3.33 f_C$, and an intermediate case with $b = 0.5$ gives $R = 2.17 f_C$.

Finally, in optically thick tori, the covering factor may also be related to the narrow-line intensities, because the smaller the covering factor is, the larger the opening is and the more NLR gas is exposed to radiation from the central source. As shown in Section 5, this is a somewhat simplistic approach because the NLR gas does not necessarily fill the entire cone and because absorption by dusty interclump material close to the edges of the torus cannot be neglected. Moreover, the intensity of the narrow emission lines relative to the bolometric luminosity, L_{AGN} , increases with decreasing source luminosity in a way that seems completely unrelated to the covering factor of the torus.

3. TORUS OBSERVATIONS

The large number of successful IR space missions of the past 20 years, the ongoing successful X-ray missions, and the significant improvements in ground-based interferometry have revolutionized the study of AGN tori. They provide huge data sets that can be used to obtain reliable IR SEDs, allow multiwavelength studies of many thousands of AGNs, and enable researchers to probe regions near the BH that are 1 pc in size. This section describes these developments and their application to individual AGNs. The related redshift and luminosity dependences are discussed in Section 7.

3.1. The Inner Torus Boundary: Dust Reverberation Mapping

The variable luminosity of the central source results in time-dependent heating and ionization of the surrounding gas and dust that can be used to obtain valuable information about the geometry and physical conditions of these regions. Reverberation mapping (RM) has been used for years to map the distribution of the line-emitting gas, mostly $\text{H}\beta$, in the BLR (line RM; see Kaspi et al. 2000, Bentz et al. 2013, and references therein). Other experiments measured the time-dependent dust emission in the NIR, mainly in the K-band, in response to the variable continuum (dust RM; see, e.g., Glass 1992, Suganuma et al. 2006, Kishimoto et al. 2007, Koshida et al. 2014, Pozo Nuñez et al. 2014). The K-band wavelength, approximately $2.2 \mu\text{m}$, is close to the peak emissivity of the hottest dust and the experiments provide information about the inner torus boundary (Section 1.2).

The main result of dust RM experiments, now carried out successfully in approximately 20 low-to medium-luminosity AGNs, is a tight correlation of the form $R_{2.2 \mu\text{m}} \simeq 0.4(L_{46})^{1/2}$ pc (Koshida et al. 2014), where $L_{46} = L_{\text{AGN}}/10^{46} \text{ erg s}^{-1}$, and I converted the measured V-band luminosity to L_{AGN} assuming $L_{\text{AGN}} \simeq 8\lambda L_{\lambda}(5,500) \text{ \AA}$. Thus, to a good approximation, $R_{2.2 \mu\text{m}} = \langle R_{\text{sub,C}} \rangle$ (Equation 1). Note, however, that different values for the dust sublimation radius have been used in the literature (e.g., Koshida et al. 2014), which led to suggestions that the measured V-K time lag is two to three times smaller than the time lag expected from sublimation temperature considerations. The comparison of the $\text{H}\beta$ and K-band RM results is shown in **Figure 4**. The measured K-band time lag is three to four times longer than the $\text{H}\beta$ time lag, a result that is expected given what we know about gas and emissivity distributions in the BLR (Netzer 2013).

RM experiments are not without difficulties. The dust transfer function (i.e., the dust emission in response to a delta-function central source light curve) must be complicated and differs substantially from a simple thin or thick shell. For example, it depends on the torus and disk inclination, the dimming of disk radiation toward its equatorial plane, and the occultation of some parts of the torus (Kawaguchi & Mori 2010, 2011; Pozo Nuñez et al. 2014). Nevertheless, the agreement

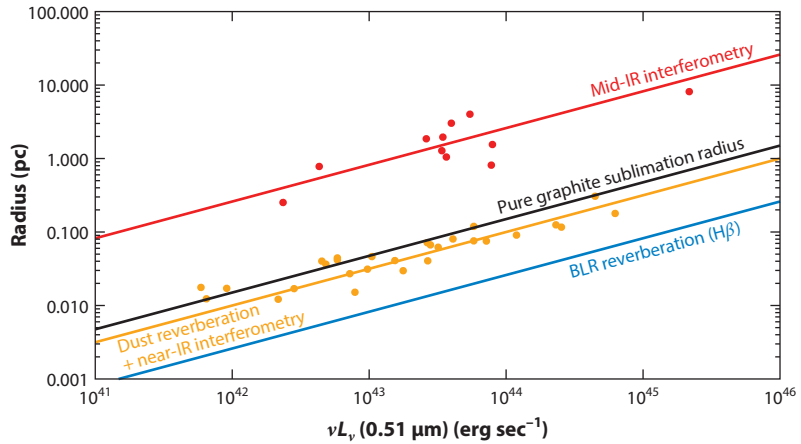


Figure 4

Various measures of the size of the central torus. MIDI-based measurements of $R_{1/2}$ (red points, red line), measurements based on dust RM that use V- and K-band light curves and K-band interferometry (orange points, orange line), graphite sublimation radius from Equation 1 (black line), and the H β RM size (blue line). The typical torus size obtained from the 8–13 μm observations is approximately 30 times larger than the size estimated from dust RM experiments. Figure adapted from Bartscher et al. (2013), courtesy of L. Bartscher. Abbreviations: BLR, broad-line region; MIDI, mid-infrared instrument; RM, reverberation mapping.

between the RM results for dust and the predicted graphite sublimation radius suggests that the inner torus wall is determined by the maximum grain temperature.

Two comments about the relative sizes of the BLR and the inner torus walls are in order. The H β radius measured by RM experiments should not be mistaken for a single-location BLR. In fact, the more successful BLR models require the ionized dust-free gas to extend from the inner disk to the torus (e.g., Mor & Netzer 2012). In addition, the quoted distance ratio of 3–4 is only an average; actual ratios range from 1.5 to approximately 10. This range reflects the uncertainties of individual measurements and the likely large scatter in RM-based distances.

3.2. Torus Properties: SED Fitting

The various torus models of Section 2 make specific predictions about the emitted SED that can be compared with NIR–MIR observations. This SED fitting has been an active area of research because of several successful space missions, mostly *Spitzer* and the *Wide-Field Infrared Survey Explorer* (*WISE*). The satellite data are supplemented with ground-based J-, H-, K-, L-, and N-band observations with inferior wavelength coverage but much superior spatial resolution. The spectroscopic characteristics of the torus that allow researchers to distinguish type-I from type-II SEDs are the 9.7 and 18 μm silicate features and the 1–8 μm continuum slope. The comparison between observations and theory discussed below is biased toward phenomenological models because they were used in almost all such studies.

The spatial resolution of the IR observations is of great importance because galactic scale emission dilutes the characteristic signature of the torus. Stellar emission can contribute to the signal observed at NIR wavelengths, and dust emission from SF regions can dilute the torus signature at 10–30 μm . In particular, strong polycyclic aromatic hydrocarbon (PAH) features, mostly at 6.2, 7.7, and 11.3 μm , can contribute significantly to the MIR emission and dilute

broad-band photometric observations. In addition, dust emission from the NLR can contribute significantly to the 10–30 μm continuum (Schweitzer et al. 2008, Mor et al. 2009, Mor & Netzer 2012). Because of this, small-aperture spectroscopic observations are preferred. Unfortunately, the *Spitzer* spectroscopic apertures are several arcseconds in size and include significant contribution from the host galaxy in low-luminosity AGNs (see Buchanan et al. 2006 for a large collection of such contributions). Alonso-Herrero et al. (2011) and Lira et al. (2013) compare in great detail large- and small-aperture spectroscopic observations.

Ramos Almeida et al. (2011, 2014) provide high spatial resolution (approximately 35 pc), detailed observations of a very small number of objects. The results are similar to results in other studies by this group and claim to be clean because they avoid galaxies with known dust lanes that affect the SED shape and the depth of the 9.7 μm feature. The 1.5–19 μm SEDs obtained in those studies indicate a considerably different slope for the two types of AGNs. For type-I AGNs, $\lambda L_\lambda \propto \lambda^{0.7}$, and for type-II AGNs, $\lambda L_\lambda \propto \lambda^{1.6}$, with a rather large scatter in both slopes. However, Lira et al. (2013) used a much larger sample of type-II sources and their work disagrees with some of the results of Ramos Almeida and colleagues. Lira et al. show a very large range of slopes, including some that are similar to and even flatter than the type-I slopes found by Ramos Almeida et al. (2014). It seems that there is no canonical NIR–MIR slope for low-luminosity type-II AGNs.

Most attempts to derive torus parameters, such as the number of clumps along a certain direction and clump optical depths, give inconclusive results. Lira et al. (2013) compared in detail the rather different clumpy torus models of Nenkova et al. (2008b) and Stalevski et al. (2012) and obtained statistically satisfactory fits for both. One parameter of the fit is the inclination angle, but unfortunately no correlation between the angles was found by applying the two models. Lira et al. (2013) also found that SED fitting of approximately half of their type-II sources requires an additional very hot dust component, with a dust temperature of approximately 2,000 K, to explain the flux observed in the NIR band. None of clumpy models used in this work included such hot dust. It seems that the NIR–MIR spectra of all types of AGNs do not contain enough spectral features to distinguish one object from the next, or one clumpy torus model from another. In other words, torus models contain enough free parameters to fit almost any observed SED.

There are several examples of SED fitting of luminous, type-I AGNs (Schweitzer et al. 2008, Mor et al. 2009, Assef et al. 2013, Lusso et al. 2013, Roseboom et al. 2013). Schweitzer et al. (2008) demonstrated that successful SED fitting of large-aperture observations requires, in addition to the standard torus model, very hot, $T > 1,500$ K, emission from the torus and warm dust emission from the NLR. This approach was later used by Mor & Netzer (2012), who combined the Nenkova et al. (2008b) clumpy torus model with pure graphite grains and a dusty NLR. The hot dust component is not an integral part of the Nenkova et al. (2008b) models and its treatment is rather simple. After subtracting the host SF contribution, they fitted *Spitzer* spectra combined with NIR photometry and obtained satisfactory fits, similar to those shown in **Figure 5**, for more than 100 medium- and high-luminosity AGNs. The composite SED of this sample (red line in **Figure 3**) indicates a very flat, slope zero (in λL_λ) 2–25 μm continuum and a turndown at longer wavelengths. The exact dependence of a long wavelength is sensitive to the assumed SF contribution. Indeed, a parallel effort by Mullaney et al. (2011), who used a smaller sample of AGNs of both types, suggested a decline that starts at a longer wavelength of 30–40 μm . As shown above (**Figure 3**), a simple combination of a few large clumps can fit such observations almost as well as the sophisticated clumpy models can.

The Mor & Netzer (2012) SED fittings were used to constrain the various parameters of the clumpy torus model of Nenkova et al. (2008b). The results show a well-defined inner radius, an ill-defined outer radius, and a broad distribution of cloud properties. Many of these properties are

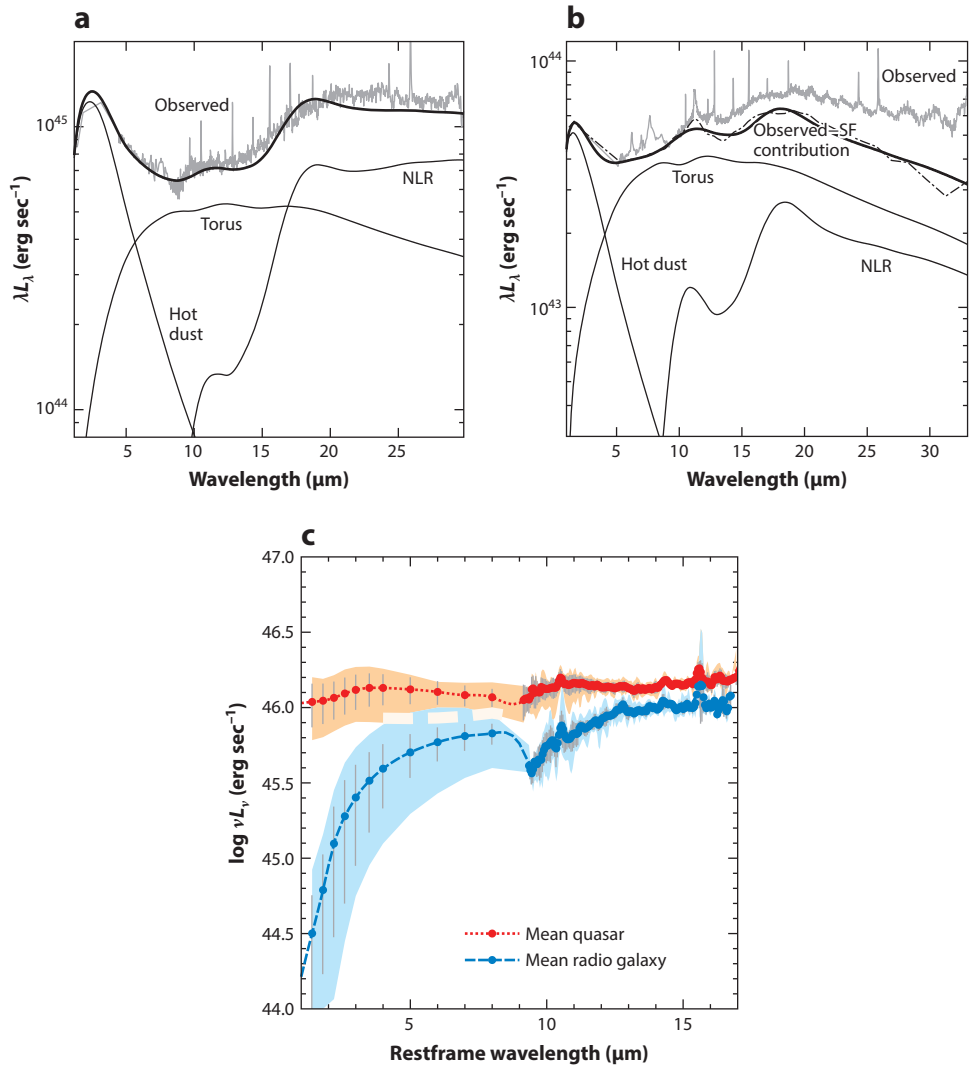


Figure 5

(a,b) Observed (gray) and SF-contribution-subtracted (dot-dashed line) SEDs of two type-I AGNs. The diagrams show the three components used in the fit: hot pure graphite dust, a clumpy torus model with ISM-type dust, and dust emission from the NLR. The thick black curve is the sum of the three components. Adapted from Mor & Netzer (2012) with permission. (c) Composite type-I (quasars) and type-II (radio galaxies) SEDs of $z \sim 1.2$ steep spectrum radio-loud AGNs, illustrating the large spectral differences between the two groups. Reprinted from Hönig et al. (2011) with permission. Abbreviations: ISM, interstellar medium; NLR, narrow-line region; SED, spectral energy distribution; SF, star forming.

similar to those found by Lira et al. (2013) when fitting their own type-II objects. The fittings also allow researchers to compare how the three major components contribute to the total dust emission. For the luminosity median of the population, $L(\text{hot torus dust}):L(\text{warm torus dust}):L(\text{NLR dust}) \approx 40:40:20$. The relative NIR and MIR luminosities in the Roseboom et al. (2013) sample, which does not consider the NLR contribution, are similar and somewhat luminosity dependent.

The fits also provide an estimate of the luminosity-dependent size of the NLR:

$$R_{\text{NLR}} \simeq 460 \left[\frac{L_{\text{AGN}}}{10^{46} \text{ erg s}^{-1}} \right]^{0.67} \text{ pc.} \quad (6)$$

This dimension is more than two orders of magnitude larger than the silicate sublimation radius and is in agreement with the inner part of the NLR derived from direct imaging and photoionization models. It corresponds to a mean grain temperature of approximately 160 K with a peak emission at approximately 18 μm .

An additional detailed study of the NIR–MIR SED of $z \sim 1.2$ luminous radio-loud AGNs covers the rest-frame wavelength of 1–17 μm (Hönig et al. 2011). The sample includes 3CRR sources originally described by Haas et al. (2008) and Leipski et al. (2010) that are similar in their IR–optical–UV properties to radio-quiet AGNs. Despite its small size (20 objects), the sample is most suitable for the comparison of type-I and type-II sources because it is chosen on the basis of the extended radio emission, which is expected to be radiated isotropically. Although the mean radio luminosity of the two groups is almost identical, the NIR–MIR spectrum is different (see **Figure 5**). The type-I SEDs (called quasars in the figure) are flat in λL_λ and similar to the Mor & Netzer (2012) composite. The type-II SEDs (called radio galaxies) rise steeply from 1 to 7 μm and are similar to some of the type-II SEDs discussed above.

In summary, the typical NIR–MIR SEDs of type-I and type-II AGNs are rather different. Most but not all type-I AGNs show significant hot dust emission. Type-II AGNs show a much larger diversity in which some objects are similar to type-I AGNs and others show a steep decline from long to short wavelengths. Clumpy torus models provide adequate fits to many observed SEDs but seem to be degenerate with respect to their basic parameters. Because of this, models with different geometry, dust distribution, and even inclination can produce equally good fits to the same data. The inner region of the torus, which contains pure graphite dust, is required by the observations but is missing from today’s models. Given all this, it is not yet clear that current phenomenological models resemble, well, real AGN tori.

3.3. Anisotropy and Covering Factor

As explained in Section 2.3.2, dust emission from optically thick tori is characterized by a wavelength-dependent anisotropy. Several of the torus models described in Section 2 are optically thick throughout most of the 1–20 μm wavelength range, and SED differences between type-I and type-II sources can be used to derive the anisotropy. According to Hönig et al. (2011), the anisotropy is the cause of the different SEDs shown in **Figure 5c**. In this particular case, if the type-II inclination angle is 75° and the type-I inclination angle is 39° , the column density needed to produce this anisotropy corresponds to $A_V \sim 150$ mag. Even at such a large column, the optical depth is small and the emission is isotropic at $\lambda \geq 30 \mu\text{m}$.

A direct way to estimate the anisotropy is to measure the dust optical depth by searching for broad Paschen and Brackett lines in the spectrum of type-II sources. The total number of objects studied in this way is small (see Lutz et al. 2002 and references therein) and the typical detection rate is only approximately 30%. The most useful results were obtained for type-II AGNs showing broad Balmer lines in polarized light, indicating a hidden BLR. The handful of broad Br α lines reported by Lutz et al. (2002) indicate that $\tau(4.05 \mu\text{m}) \sim 3$ mag., corresponding to column densities of the order of 10^{23} cm^{-2} , which are consistent with the columns derived from X-ray observations of the same sources. For several objects in this sample, with polarized broad emission lines but no direct broad-line detection at 4.05 μm , the obscuration must be larger. As shown in Section 4, such a good agreement is not typical of many AGNs.

The large NIR optical depths deduced from the Br α observations should not be confused with the observations of many type-I AGNs showing weak broad H α lines and basically no broad H β lines, indicating a few magnitudes of visual extinction. Such objects are common, estimated to compose 10–20% of all low-redshift AGNs (e.g., Lawrence & Elvis 1982, Antonucci 1993, Elvis 2012; see Section 1). They are thought to be reddened by galactic scale dust, although in some cases the source is probably seen through a small-column-density part of the torus. Reddening of high-luminosity high-redshift AGNs is also a common phenomenon (e.g., Glikman et al. 2004, Lacy et al. 2007). Such objects are found in IR and radio surveys, and their weak, occasionally undetected optical emission suggests a large range of dust extinction, from that typical of many local type-I sources to much higher. The fraction of such objects in the general population must be high but is not accurately known.

Anisotropy influences covering factor estimates on the basis of the measured $L_{\text{dust}}/L_{\text{AGN}}$ (Equation 5). The estimation of the mean and the distribution of f_c requires an additional correction that takes into account that a given L_{AGN} is associated with a range of covering factors. In particular, a large f_c increases the probability of classifying a source as type-II and the opposite is true for type-I sources (Equation 4).

Covering factors for a large number of type-I AGNs have been obtained by using the $L_{\text{dust}}/L_{\text{AGN}}$ method (Maiolino et al. 2007, Treister et al. 2008, Mor & Trakhtenbrot 2011, Mor & Netzer 2012, Lusso et al. 2013, Roseboom et al. 2013). The quality of the SED fits in such studies ranges from poor to very good, where spectroscopy-based fits provide more reliable measurements. Not all studies include the anisotropy correction term, which results in overestimation of f_c . All studies show a broad distribution of f_c for a given luminosity, with a type-I population mean of 0.3–0.6. There are indications that the mean covering factor decreases with increasing source luminosity, but this result depends on the method used to estimate L_{AGN} , which varies considerably between studies. Some of the studies attempted to separate hot (NIR) from warm (MIR) dust (Mor & Trakhtenbrot 2011, Mor & Netzer 2012, Roseboom et al. 2013). They showed that the hot-dust covering factor varies over a larger range, with some sources missing this component altogether (hot-dust-poor AGNs; see Mor & Trakhtenbrot 2011). The fraction of such sources among luminous AGNs is approximately 15%. In general f_c (hot dust) \approx f_c (warm dust), but the separation of the two is model dependent. A big disadvantage of this method as applied to IR-selected samples is the bias against low-covering-factor sources.

The covering factor of the torus can be obtained directly from modeling the observed X-ray continuum (see Section 1). Ueda et al. (2007) and Brightman & Ueda (2012) demonstrated this by carefully comparing the scattered and transmitted X-ray flux of a large number of type-II AGNs. The authors claimed to measure scattered radiation, which is as low as 1–2%, and thus identify buried active BHs that are completely surrounded by geometrically thick tori with $f_c \simeq 1$. Their work suggests that some 20% of high-redshift sources in several deep X-ray fields are completely buried AGNs.

An additional way to estimate f_c is based on the observed intensity of the narrow Fe K α line (Section 1.2). Studies of large X-ray samples show that EW(K α) decreases with increasing X-ray luminosity, roughly like $L_{\text{AGN}}^{-0.15}$, but not with redshift (the X-ray effect; see, e.g., Iwasawa & Taniguchi 1993, Chaudhary et al. 2010, Ricci et al. 2013). EW(K α) depends on the combination of the torus column density, covering factor, and metallicity (Ikeda et al. 2009, Yaqoob et al. 2010, Brightman & Nandra 2011a, Ricci et al. 2013). The advantage of this method is that the selection of sources by their X-ray flux is independent of the measured quantity, EW(K α). Possible complications are extra emission from K α produced in broad-line clouds and the fact that EW(K α) also depends on column density. Moreover, the measured LOS X-ray column and the mean column density of the torus are not necessarily the same (see, e.g., Brightman & Ueda 2012).

Finally, a complementary approach to finding a population mean covering factor is to measure the LOS-obscuring column and associate small columns with type-I sources and large columns with type-II sources. The mean f_C is then obtained from the $N_{\text{type-II}}/N_{\text{type-I}}$ ratio, where N is the number of objects. This method is discussed in Section 7.

Weedman et al. (2012) examined the covering factor of the most luminous AGNs; they compared the *WISE* (rest-frame 7.8 μm) and SDSS (rest-frame wavelength of 1,350 \AA) luminosities of the most MIR-luminous type-I AGNs at redshifts of 1.5–5. The study assumed $L_{\text{dust}}/L(7.8 \mu\text{m}) \simeq 3$ and found extremely high values of L_{dust} , $10^{46.9-47.3} \text{ erg s}^{-1}$, and $f_C > 1$ for many sources. The problem with this and several other studies is the neglect of known selection effects and necessary correction factors, such as the anisotropy correction term of Equation 5 and the possible anisotropy of the accretion disk radiation. Moreover, these objects are probably unique among type-I AGNs in terms of their covering factor because they were selected to be the most IR luminous. The agreement between the luminosity distributions at 7.8 μm and 1,350 \AA is indeed poor. Finally, a large fraction of the sources may be reddened because of the large dust covering factor, a possibility acknowledged by the authors. Taken together, it seems that the mean covering factor of the torus for the most luminous type-I AGNs is approximately 0.5.

An important way to evaluate the combined effect of anisotropy and covering factor is to compare the X-ray and MIR luminosities, $L(\text{MIR})/L(2-10 \text{ keV})$. The comparison made at 6 and approximately 12 μm shows an almost identical mean ratio for the two AGN types, over four orders of magnitude in luminosity, with a typical scatter of approximately 0.3 dex (Lutz et al. 2004, Gandhi 2009, Levenson et al. 2009, Hönig et al. 2010, Asmus et al. 2011, Brightman & Nandra 2011b, González-Martín et al. 2013, Merloni et al. 2014). This is a somewhat surprising result given the covering factor and anisotropy discussed above. Naive expectations suggest on the one hand that the larger covering factor of type-II sources would increase the ratio $L(\text{MIR})/L(2-10 \text{ keV})$ relative to that of type-I sources. On the other hand, anisotropy of the MIR emission would tend to decrease this ratio in type-II AGNs typically seen at higher inclination angles. Emission by NLR dust will affect large-aperture observations and will contribute equally to the two types. This cannot be a significant source of confusion at 6 μm , where the NLR dust contribution is small, or when using small-aperture observations that exclude most of the NLR emission. Is it possible that all these effects conspire to smear out the differences between type-I and type-II AGNs? There were several attempts to blame the method used to estimate $L(2-10 \text{ keV})$ for the unexpected constant ratio of $L(\text{MIR})/L(2-10 \text{ keV})$ (Brightman & Nandra 2011b, LaMassa et al. 2011, Mayo & Lawrence 2013) and to obtain absorption-corrected X-ray luminosities that take into account more complex clumpy tori, including partial covering in some directions. However, it is difficult to determine how all this can explain the above luminosity ratio.

3.4. Imaging Interferometry

The most important development regarding AGN unification is perhaps the significant improvements in long baseline interferometry and the ability to resolve the central structure on a milliarcsecond scale. The most significant results were obtained by three instruments. The first is the mid-infrared instrument (MIDI) from the European Southern Observatory (ESO). This interferometer operates in an atmospheric window of 8–13 μm , with projected baselines ranging from approximately 30 to 130 m (e.g., Jaffe et al. 2004, Kishimoto et al. 2011b, Burtscher et al. 2013, Hönig et al. 2013). This instrument provided the largest sample. The second instrument is the Keck K-band interferometer (KI) (see Swain et al. 2003, Pott et al. 2010, Kishimoto et al. 2011a), with a projected baseline of 85 m. The third instrument is the ESO Astronomical Multi-BEam combineR (AMBER) (Weigelt et al. 2012). Interferometric measurements allow measures

and models of the size and shape of the IR-emitting components on a spatial scale of less than 1 pc. The attainable resolution depends on the flux distribution in the source, the wavelength and baseline of the experiment, the redshift, and the source coordinates (which determine the coverage of the uv-plane). The results are often quoted in units of $R_{1/2}$, which is the wavelength-dependent radius containing half of the emitted flux. The latest results from MIDI, summarized in Burtscher et al. (2013) and illustrated in **Figure 4**, include 23 sources with 8–13 μm dimensions of 1–100 pc. The KI and AMBER samples are smaller but provide valuable information about shorter wavelengths and hotter dust.

The large scatter in the measured $R_{1/2}$ at MIR wavelengths is different from the tight correlation between size and luminosity indicated by dust RM that probes regions closer to the inner torus boundary. Part of this must be related to the fact that in many cases, there are two distinct components in the resolved N-band interferometry. Translating this to a specific size is obviously model dependent and subjected to large uncertainties. All this indicates a rather complex relationship between radius and dust temperature in the torus. Another surprise is the similar size of type-I and type-II objects of the same luminosity (simple tori predict that type-II tori will look larger). Furthermore, the measured K-band $R_{1/2}$ is larger, by 0.2–0.4 dex, than the K-band size measured by RM (Kishimoto et al. 2011a). This is likely related to the different definitions of the two radii, as $R_{1/2}$ is a flux-weighted radius and R_{in} (or R_{sub}) is a response-weighted radius.

In a small number of well-observed nearby sources, the interferometry allows researchers to obtain model images that reveal the rough structure, elongation, and inclination of the central dusty structure. As of 2014, we have this information for four sources: NGC 1068 (type-II), Circinus (type-II), NGC 424 (type-I), and NGC 3783 (type-I). Of the four, the spatial information obtained for the Circinus galaxy, a type-II AGN with a graphite sublimation radius of approximately 0.01 pc, is perhaps the best. The emissivity maps of this source, in three MIR bands, were modeled by Tristram et al. (2014) and their combination is shown in **Figure 6**. The figure also shows the boundaries of the ionization cone based on HST imaging of the [O III] $\lambda 5007$ line. The map shows two distinct components. The first is a thin (axial ratio of 1:6 or less), approximately 1 pc disk-like structure, emitting approximately 20% of the MIR flux, with an orientation that agrees with the orientation of the smaller (0.1–0.4 pc) warped maser disk observed in this source (Greenhill et al. 2003). The second is a much larger and thicker elongated structure, roughly perpendicular to the first component. This ellipse-shaped component, elongated roughly in the polar direction, emits approximately 80% of the 8–13 μm flux with a clear wavelength gradient reflecting the dust temperatures in the various parts. None of these features is in agreement with the shape and orientation of a simple central torus.

An exciting result is obtained by combining MIDI (N-band) and AMBER (K-band) measurements of the type-I AGN NGC 3783. The combined model image indicates different elongations of the K- and N-band isophotes. The K-band model image (which is still somewhat uncertain) likely elongates in a direction parallel to the expected plane of the torus. The N-band model image is of much larger dimensions and is elongated almost perpendicular to the K-band model image, along the expected polar axis. Hönig et al. (2013) interpreted this geometry as a combination of an inner small torus with very hot dust and a dusty polar outflow that, because of its distance, contains cooler dust. This interpretation is somewhat similar to that of the Circinus model mentioned above (for which K-band information is not available). Earlier ground-based adaptive optics–assisted observations pointed out polar emission in a different source (NGC 1068; see Bock et al. 2000).

Although complicated radiative transfer effects may result in the unusual model images presented here (see Schartmann et al. 2005), the interferometric results for Circinus and NGC 3783,

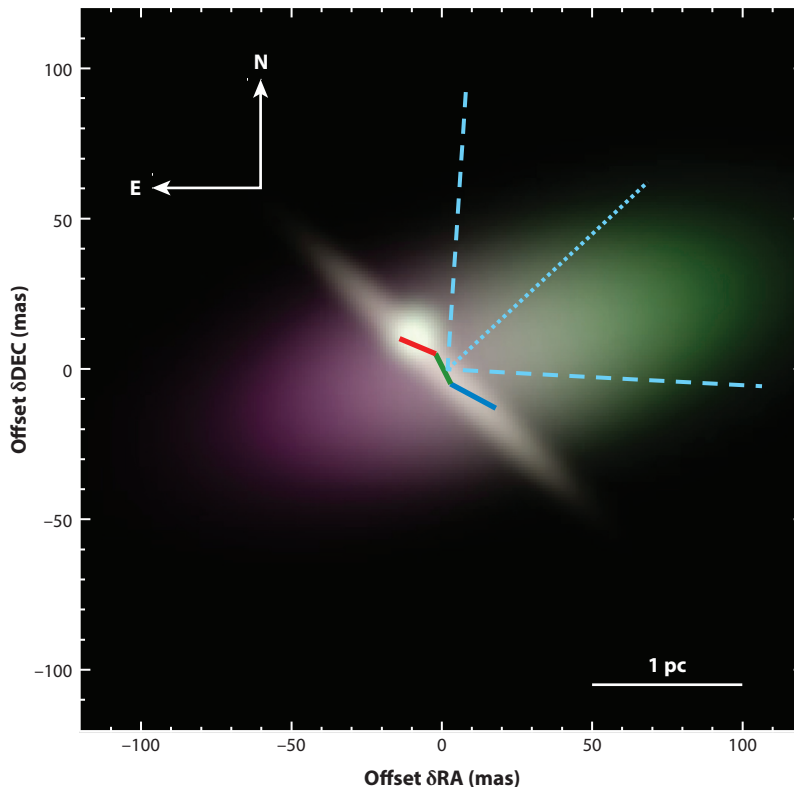


Figure 6

A MIDI-based model image of the Circinus galaxy showing the location of the maser disk (*red-green-blue line*); central thin MIR-emitting structure (*white*); and a larger, thick, elongated structure, with colors marking central wavelengths: red, 13 μm ; green, 10.5 μm , and blue, 8 μm . The thick red-green-blue elongated structure emits approximately 80% of the MIR radiation. Its orientation is different from the expected orientation of a standard torus. The boundaries of the ionization cone (only one side in this source) are shown as dashed blue lines (adapted from Tristram et al. 2014, courtesy of K. Tristram). Abbreviations: MIDI, mid-infrared instrument; MIR, mid-infrared.

and indications for similar structures in two other sources, suggest a possible change of paradigm. A central, equatorial, small-covering-factor torus may still be needed to explain the hot dust emission, but much of the cooler, approximately 300 K dust may well reside in an additional component that has different geometry, size, and optical depth, and perhaps different dynamics (i.e., a wind component). A realistic model for this new structure must combine several different elements and take into account that the hotter inner torus must also emit some of the observed MIR flux (e.g., 20% in the case of Circinus). Such a model should also answer several outstanding questions about the clear pass to the ionization cone, indicated by strong unreddened narrow lines if the flow is optically thick or by the lack of silicate emission in the Circinus spectrum if it is optically thin. It must also dismiss covering factor estimates that apply only to simple axisymmetric tori. In particular, the assumption of $f_c(\text{total}) = f_c(\text{hot dust}) + f_c(\text{warm dust})$ may not work in this type of geometry. Finally, several hydrodynamic models suggest dusty polar outflows (Wada 2012), which may partly explain the observations.

4. ADDITIONAL AND ALTERNATIVE OBSCURERS

4.1. Galactic Scale Obscuration

Galaxy-scale obscuration is common in many AGNs, and numerous individual cases studied by HST and ground-based observations have been documented since the 1980s (e.g., Lawrence & Elvis 1982, Antonucci 1993, Malkan et al. 1998, Prieto et al. 2014). Well-known examples are some of the objects detected by optical spectroscopy and classified here as type-Ii AGNs. In several past publications they were called narrow-line X-ray galaxies (NLXGs). Some of the objects show kiloparsec-scale dust lanes, others might be affected by dust in the torus. The fraction of type-Ii AGNs might have been underestimated because many real type-II AGNs (Merloni et al. 2014), especially those for which spectroscopic observations were of low quality, may belong to this group. As argued in Section 7, this group is a major source of uncertainty when estimating the relative fractions of AGNs that are type-I and type-II.

Galactic scale obscuration is more common in low-luminosity type-II AGNs. High spatial resolution observations of such objects reveal kiloparsec-scale dusty filaments that seem to be connected to much smaller dusty features close to the nucleus. This finding led Prieto et al. (2014) and others to propose that a central torus is not required for AGN unification at low luminosity. Large-scale LOS absorption has also been found in several Compton-thick AGNs studied with *Spitzer* (Goulding et al. 2012). In this sample, AGNs in face-on galaxies show little silicate 9.7 μm absorption, as predicted by clumpy torus models, and AGNs in nearly edge-on galaxies, or in mergers, show much stronger silicate absorption, indicating dust in the galaxy. This finding adds to previous similar results obtained for Compton-thin type-II AGNs (Deo et al. 2007, 2009). In some cases, galactic extinction is so large that it can completely obscure the central AGN at optical wavelengths (Goulding & Alexander 2009). The connection, if any, to the heavily reddened AGNs mentioned above is not yet clear.

Supplementing the detailed investigation of individual sources are lower spatial resolution studies of many thousands of AGNs such as that by Lagos et al. (2011). This study finds that spiral and elliptical type-I hosts are strongly skewed toward face-on inclinations, whereas type-II hosts are skewed toward edge-on inclinations. The study also shows that galactic dust absorption by itself cannot explain the absence of broad emission lines in type-II sources. The inclination of the host galaxy strengthens the idea that the angular momentum of the material that feeds the BH retains a memory of its origin in the galaxy; i.e., statistically speaking, galaxy disks, central tori, and inner accretion disks, are generally aligned. This issue, which was investigated in numerous papers, remains unresolved. For example, Kinney et al. (2000) used information from radio jet position angles and claimed to find no correlation between jet direction (i.e., orientation of the inner accretion disk) and the disk of the host galaxy.

4.2. X-Ray Obscuration by Gas in the BLR

The simple idea of a single torus-like obscurer suffers from various limitations, especially where very large column densities are concerned. For example, the observed optical reddening is much smaller than the value obtained by translating the measured X-ray column to foreground extinction, assuming galactic dust-to-gas ratio (e.g., Maiolino et al. 2001, Risaliti et al. 2002, Goulding et al. 2012). In addition, some X-ray variations indicate large changes in the obscuring column on short timescales (a few days or less), which is not consistent with the idea that the obscuring material is outside the sublimation radius. This inconsistency raises the possibility that obscuration by dust-free gas inside the BLR affects X-ray absorption and hence AGN classification.

The typical dimensions of BLR clouds are estimated to be 10^{13-14} cm and their typical column density is of the order of 10^{23-24} cm $^{-2}$. This is roughly the size of the central X-ray source in low-to intermediate-luminosity AGNs (a few R_g). For an X-ray continuum source approximately 10^{14} cm across, and a cloud velocity of the order of $3,000$ km s $^{-1}$, the occultation time is of the order of 4 days. Can such clouds occult the central source, giving the impression of a variable X-ray source? Recent observations and modeling suggest that this is indeed the case for almost every object for which the observations are of a long-enough duration to discover such eclipses.

Detailed studies of a small number of type-I and type-II AGNs provide evidence for eclipses by large-column-density blobs (Risaliti et al. 2007, 2011). In the best-studied case, NGC 1365, the X-ray source underwent a total eclipse in less than 48 h and then emerged within the same time (Risaliti et al. 2007). Detailed modeling of this and similar events by Maiolino et al. (2010) provided information about the likely location, velocity, and size of the occulting gas, all of which were consistent with being part of the BLR and inside the sublimation radius. Maiolino et al. (2010) speculated that the occulting clouds might have developed cometary tails, which are manifested as a gradual decrease in the column density as clouds emerged from the eclipse. Different time-dependent X-ray absorption events from inside the sublimation radius are described in Turner & Miller (2009).

More studies, though not as detailed, include a larger number of AGNs and occultation events. The work of Markowitz et al. (2014) is based on long-term monitoring of approximately a dozen AGNs of both types. These objects were monitored continuously by the *Ross X-ray Timing Explorer* and the total duration is of the order of 10 years. Given the known BH mass in these sources, one can calculate the expected crossing time of dusty and dust-free blobs of certain properties at different locations. The results suggest that many of the clumps are indeed inside the sublimation radius, with properties consistent with those of BLR clouds. Other blobs are larger and move slower, with locations consistent with being inside the dusty torus. In several of the cases the clump location, assuming Keplerian orbits, seems to be close to the maximum allowable dimension of such tori. Markowitz et al. (2014) also presented an analysis of the nonvariable X-ray-absorbing columns and claimed they conflict with the predicted dimensions, column density, and number of clumps in clumpy torus models. An additional study by Torricelli-Ciamponi et al. (2014) includes more sources but shorter-duration monitoring, sensitive to events that last a few days at most. It presents numerous events associated with changes to hardness ratio of the X-ray continuum, all consistent with being caused by transiting blobs inside the BLR. The observations are not detailed enough to allow a robust determination of the column density of the absorbers.

The X-ray observations beautifully illustrate the connection between dust-free and dusty clumps in one general region that contains the BLR closer to the central BH and the torus farther away from the central BH. The earlier apparent disagreement between optical reddening and X-ray column density disappears when accounting for the combination of inner dust-free and outer dusty absorbers. The observations also help explain the nature of some of the largest obscuring columns found in AGNs.

4.3. Tilted Disks

Is an axisymmetric torus-like structure the only type of central obscurer that can explain the various aspects of AGN unification? Can other structures help resolve several known disagreements between simple torus models and observations? An interesting scenario is based on the idea that a central disk can replace the torus (Lawrence & Elvis 2010). This ad hoc phenomenological model posits that the angular momentum of the external inflowing gas is initially misaligned with the axis of the central accretion disk. The misalignment is kept down to small distances, of the order

of 1 pc, and the inflow takes the form of an inclined, large, dusty, geometrically thin disk, which may also be warped (see Caproni et al. 2006 for general mechanisms resulting in warped disks). The large disk presents a wide solid angle to the inner disk and part of the UV-optical radiation is absorbed and reemitted in the IR. Lawrence & Elvis (2010) used this simple geometry to predict the distribution of the covering factor, which was later studied by Roseboom et al. (2013), who used *WISE* data of a large type-I sample. There seems to be reasonable agreement between the model and observations, but the predicted distribution is similar to a normal distribution, which is also expected in other scenarios.

The main virtue of the tilted disk scenario is the assumed misalignment between different accretion episodes onto the BH. Misalignment is expected in accretion events for which the final stage takes place in a region that is two to three orders of magnitude smaller than the region where the flow originates. Unfortunately, the exact geometry is not consistent with realistic hydrodynamic simulations, the location of the sublimation surface has not been calculated and compared with RM results, and there is no comparison with IR interferometry, IR SED, and high-quality polarization measurements.

5. IONIZATION CONES

An axisymmetric central obscurer with a central opening results in an anisotropic two-sided conical shaped ionizing radiation pattern (bicone). Early observations (Pogge 1988, Tadhunter & Tsvetanov 1989, Mulchaey et al. 1996) identified bicones in a number of nearby systems and used them to deduce the torus inclination angles. Studies of the archetype source, NGC 1068, are the most detailed and the most detailed mapping utilized the strong [O III] $\lambda 5007$ line (the [O III] bicone). More recent studies (like Fischer et al. 2013) include larger samples, more detailed imaging in the light of more emission lines, and additional kinematic information. The mapped emission lines now include low-ionization species such as [O I], intermediate-ionization ions such as [O III] and [O IV], and very high-ionization ions such as [Si VI]. High-resolution images obtained by the *Chandra X-ray Observatory* (*Chandra*) allow researchers to map such bicones in individual X-ray lines such as [O VII].

The most detailed observations of today are based on HST imaging, HST long-slit spectroscopy, and ground-based integral field unit (IFU) studies (e.g., Müller-Sánchez et al. 2011, Fischer et al. 2013, Riffel et al. 2013, and references therein). More than 50 sources have been mapped in detail; of those, we have reliable kinematic information for more than 20. The highest redshift is approximately 0.05. The observations are detailed enough to allow photoionization modeling of the gas in different parts of the NLR, including, in rare cases, following the metallicity gradient across the source (e.g., Dopita et al. 2014).

The ability to distinguish low- from high-ionization regions across a spatially resolved NLR provides evidence for ionization outside the nominal [O III] bicone. Several well-studied cases provide evidence that the ionizing radiation in the parts producing the strongest low-ionization lines is filtered by clumpy, ionized absorbers located tens of parsecs or less from the nucleus, consistent with the torus dimension. HST imaging of NGC 4151 shows that the [O III] $\lambda 5007$ /[O II] $\lambda 3727$ line ratio is lower near the edges of the bicone than at its axis (Kraemer et al. 2008). Such filtering was suspected in earlier works, but information about the location of the filtering material was lacking (Alexander et al. 2000).

Line radiation from ionization cones can help to improve the estimate of the bolometric luminosity of type-II AGNs for which the nonstellar continuum is not directly observed. In particular, the [O III] $\lambda 5007$ line is a good indicator of luminosity because the line is strong and not affected much by stellar absorption (Heckman & Best 2014). Nevertheless, this method is

not without difficulties. The line is not a good indicator of luminosity in low-ionization AGNs such as LINERs (Netzer 2009), and it is now known that the ratio $L([\text{O III}] \lambda 5007)/L_{\text{AGN}}$ is changing with L_{AGN} (Stern & Laor 2012). Line reddening is an additional uncertainty. Reddening by dust outside the NLR depends on the source geometry and torus inclination to the LOS and is therefore different for type-I and type-II sources (line attenuation by dust inside the NLR clouds does not depend on these factors). Indeed, observations show that emission patterns are more isotropic in some lines than in others, which leads researchers to suggest that $[\text{O IV}] \lambda 25.9 \mu\text{m}$ is the best indicator of luminosity because MIR reddening is much lower (Diamond-Stanic et al. 2009, Weaver et al. 2010, Kraemer et al. 2011, Dicken et al. 2014). In fact, $I([\text{O III}] \lambda 5007)/I([\text{O IV}] \lambda 25.9 \mu\text{m})$ is typically lower by a factor of approximately 2 in type-II sources probably because of inclination-dependent reddening. Such a situation will occur naturally if the dust causing the extinction is just outside the $[\text{O III}]$ bicone and the bicone axis is closer to the plane of the sky.

Soft X-ray mapping of several NLRs supplemented by *Chandra* and *XMM-Newton* high-resolution spectroscopy indicate X-ray line emission, mostly $\text{O VII } 570 \text{ eV}$, that generally overlaps with the $[\text{O III}]$ bicone (Ogle et al. 2000, Sako et al. 2000, Kinkhabwala et al. 2002, Bianchi et al. 2006, Wang et al. 2011a). A spectacular example, showing X-ray emission up to approximately 7 kpc, in Mrk 573, is given in Paggi et al. (2012). The LOS attenuation of X-ray lines depends only on column density and metallicity, not on the dust content of the gas. Therefore, observations of X-ray lines provide an additional method to measure this column. Kraemer et al. (2011) analyzed the $\text{O VII } 570 \text{ eV}/[\text{O IV}] \lambda 25.9 \mu\text{m}$ line ratio in a sample of approximately 15 sources and claimed an attenuation of the X-ray line by a column density that is consistent with the derived amount of reddening, assuming an ISM dust/gas ratio. Although not direct evidence, this is consistent with the idea of a dusty ionized gas outside and farther away from the $[\text{O III}]$ bicone. X-ray emission is also detected in regions perpendicular to the optical bicone. This flux was interpreted as leakage through a clumpy, relatively low-column-density absorber, which may be the torus. Kreimeyer & Veilleux (2013) used optical line ratios to compare the flux emerging from the opening of the cone with the flux leaking through the torus. According to this work, the leakage amounts to 30–50% of the radiation emitted by the central source. This fraction is high and confirmation in other sources is required.

The kinematic studies provide information about the motion of the line-emitting gas inside the cones (e.g., Müller-Sánchez et al. 2011, Fischer et al. 2014). Fischer et al. (2013) presented multi-slit observations of 17 AGNs, 12 of which are type-II AGNs, with clear signatures of biconical outflows. The velocity maps allow fits to simple kinematic models, which are detailed enough to infer the inclination of the NLR to the LOS. In general, the angle of inclination is larger in type-II AGNs, consistent with the view that these sources are seen edge-on. There is no correlation in this small sample between the NLR inclination angle and the orientation of the disks of the host galaxy (see both supporting and contradicting results in sections above; this issue is not yet settled).

Kinematic modeling of ionization cones by Fischer et al. (2013) provides new invaluable information about ionization cones. They reveal a unique pattern of gas outflow $v \propto r$ out to a certain radius, approximately $630 L_{46}^{1/2} \text{ pc}$, and slowing down to zero beyond this radius. The fitted models are good enough to constrain the bicone inclination to the LOS and, in some cases, its opening angle. Another interesting finding is a strong increase of X-ray column density with increasing angular distance from the bicone axis, regardless of whether the column is neutral (type-II AGNs) or ionized (type-I AGNs). For type-I sources, in which the X-ray-absorbing gas is highly ionized (a warm absorber), the study suggests a connection between the inner walls of the torus and the origin of the X-ray ionized material. The study also suggests a correlation between MIR color and polar angle (see Section 3). For a handful of type-I sources, there is a hint for increasing FWHM($\text{H}\beta$) with polar angle. If verified in larger samples, it would indicate a rotational component for the

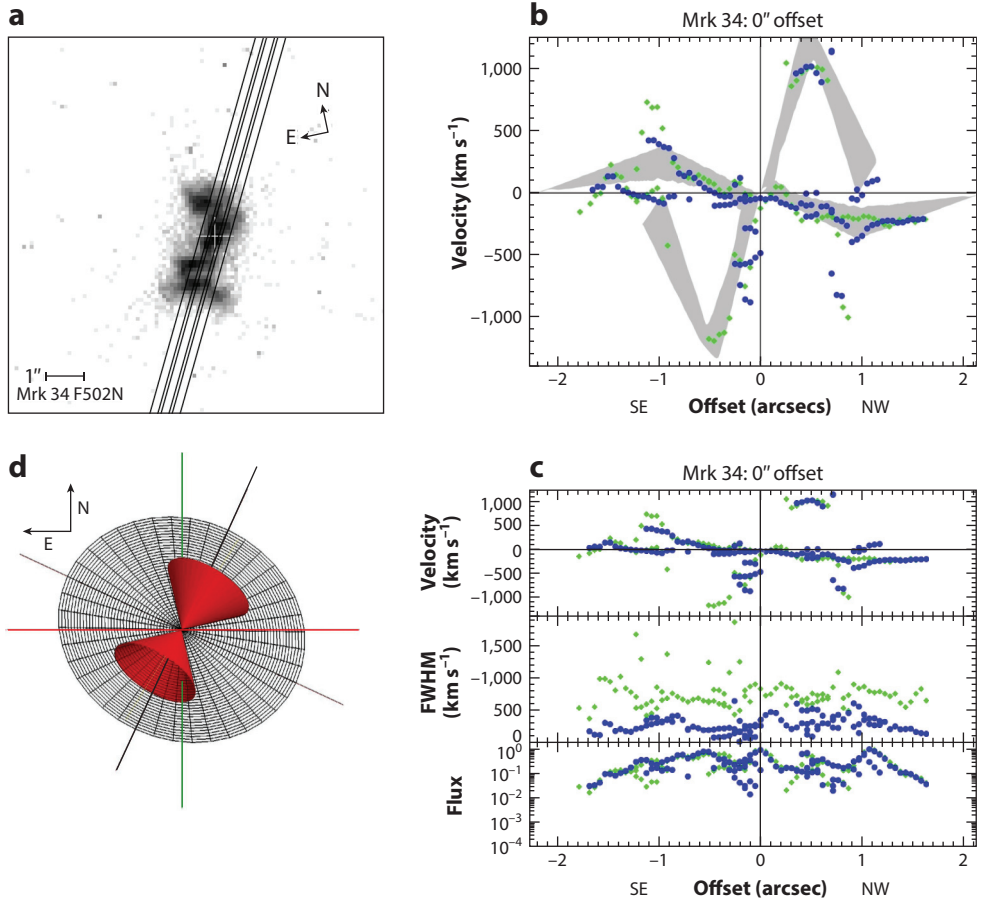


Figure 7

Kinematic mapping of the type-II source Mrk 34 showing (a) slit positions, (b,c) velocity, flux, and FWHM of [O III] $\lambda 5007$ in different positions, and (d) the resulting bicone geometry. (b,c) The green and blue points represent data obtained with the G430L and G430M gratings, respectively. Reprinted from Fischer et al. (2013) with permission. Abbreviation: FWHM, full width at half maximum.

BLR gas. Unfortunately, the results cannot be applied to the entire population partly because only one in three sources had data good enough to be modeled in this way, and partly because in some of the sources the model is based on a single-slit observation. One good case is shown in **Figure 7**.

Müller-Sánchez et al. (2011) support some but not all the findings by Fischer et al. (2013). Their work provides imaging and kinematics of the coronal line region, the innermost part of the NLR where the strongest lines are of very high ionization, e.g., [Si VI] $\lambda 1.96 \mu\text{m}$ with ionization potential of 167 eV. In this region, the gas is probably dust-free. The study of seven sources shows complex dynamics of the gas, including a rotating disk and an outflow bicone. There are agreements and disagreements between the two studies. This is illustrated in the case of NGC 3783, a well-known type-I source with a large column of LOS ionized gas and interferometric data suggesting dusty polar outflow (see Section 3). Fischer et al. (2013) modeled this source using HST imaging and a single-slit position. They found a small inclination of 15° to the LOS, as in a type-I AGN. The IFU measurements of Müller-Sánchez et al. (2011) resulted in a kinematic map

based on [Si VI] $\lambda 1.96\ \mu\text{m}$ and other coronal lines in a region close to the base of the ionization cone. They found a large inclination, close to edge-on view, with the cone opening cutting into the plane of the host galaxy. If correct, then the broad emission lines are seen through the (leaky?) torus.

In conclusion, the study of ionization cones provides valuable information about the central obscurer in AGNs. The detailed mapping in the light of numerous lines confirms the general bicone shape and shows well-defined borders between ionized and neutral gas. It also reveals the kinematics of the gas and the overall inclination to the LOS. The inferred models are more concrete and better justified experimentally than the rather vague information about the torus provided by fitting NIR–MIR SEDs.

6. THE TORUS-GALAXY CONNECTION

General scenarios linking BH feeding and SF activity have been described in numerous papers and reviewed recently in this journal by Heckman & Best (2014). These scenarios concern global galaxy properties and apply to SF activity in the central kiloparsec and beyond. They do not address the more direct connection between the two types of activity much closer to the central BH. What is known about the central 10–100 pc of nearby AGNs? What are the stellar population, the atomic and molecular gas content, and the SF activity in this region? Is there evidence for a large central disk and is it connected to the torus?

Detailed observations of the central regions in nearby AGNs shed light on some of these questions. Adaptive optics–assisted observations, as in Davies et al. (2007), can probe regions 10–30 pc in size. As of 2014, approximately 15 sources have been observed at this resolution. Esquej et al. (2014) used seeing-limited N-band spectroscopy in 29 sources and probed a region approximately 65 pc in size. The aim is to investigate SF near the nucleus using the $11.3\ \mu\text{m}$ PAH emission feature. About 45% of the objects in the sample present this feature and stacking the spectra of the remaining sources suggests its presence in many other objects. Several other works use seeing-limited optical observations, with a typical spatial resolution of 100–300 pc (e.g., Riffel et al. 2010, 2011). Important questions regarding the conditions in a region slightly larger than the size of the torus, or the sphere of influence of the central BH, are related to the age of the stellar population and the SF rate (SFR). As explained below, there is no consensus on these issues.

Standard indicators of SF are PAH features, optical absorption features, and hydrogen recombination lines. The recombination lines are the best direct indicators for ongoing SF (i.e., the presence of O-type stars). According to Davies et al. (2007, 2014), the equivalent widths of the BR_γ lines in the 15 AGNs they studied practically rule out ongoing SF and indicate post SF populations. Esquej et al. (2014) claim to detect SF activity based on the detection of PAH emission features. This apparent contradiction can be understood by noting that PAH emission is not necessarily related to the presence of O-type stars. In fact, there are indications that PAH emission is more sensitive to B-type stars than to O-type stars, i.e., to an environment that formed stars in the past 100 Myr or so (Peeters et al. 2004, Díaz-Santos et al. 2010). Moreover, the calibration of L_{PAH} versus L_{SF} used by Esquej et al. (2014) to derive the SFR is based on work by Diamond-Stanic & Rieke (2012) and Rieke et al. (2009), who used templates of SF galaxies. This calibration uses SFRs and PAH luminosities obtained through large apertures that occasionally include the entire galaxy, and is equivalent to integrating approximately 100 Myr of SF history.

Returning to AGNs, the observed PAH emission close to the center is consistent with the idea that the presently observed BH accretion episode is a few Myr old and that BH accretion might have started after the lives of all the O-type stars ended. In fact, the onset of AGN activity might have terminated all SF in the immediate vicinity of the BH, which is usually categorized as AGN

feedback (Krips et al. 2011, Davies et al. 2012, Hailey-Dunsheath et al. 2012). Additional support for the post-SF environment, and occasionally an even older stellar population close to the central BH, is obtained from other studies of the 100–300 pc central region (Riffel et al. 2010, 2011; Storch-Bergmann et al. 2012; Schnorr-Müller et al. 2014).

Some observations have sufficient spatial and spectral resolution to derive the mass and age of the stars in the inner 50 pc. In the few cases for which this was done (e.g., Davies et al. 2007), the velocity field is dominated by random motion typical of a spherical system and the stellar mass is of the order of $10^8 M_\odot$. This mass is an order of magnitude larger than the mass of the central BH in question. These observations set the stage for the stellar wind model of Schartmann et al. (2010) discussed in Section 2. The idea of BH feeding by stellar wind material has also been explored in connection with LINERs (Heckman & Best 2014 and references therein). The argument in this case is not based on spatially resolved observations but rather on the extremely low $L_{\text{AGN}}/L_{\text{Edd}}$ in LINERs. It is not at all clear whether the two independent scenarios have anything in common.

Studies of molecular gas in the vicinity of the torus do not yet have the required spatial resolution to resolve the torus, or even its close surroundings, and hence are given low priority in this review. The upcoming Atacama Large Millimeter Array observations will no doubt change this situation (see Maiolino 2008 for a review). High concentrations of molecular gas on scales of approximately 100 pc are seen in many AGNs with column densities large enough to confuse the picture of pure torus absorption. There are clear indications of outflows possibly associated with the direction of the bicone, but no indication of inflow. Some of these studies are detailed in Hicks et al. (2009), Combes et al. (2013), Aalto et al. (2015), and García-Burillo et al. (2014), in which references to older observations can be found.

None of the above observations and theoretical considerations can be applied, by simple scaling, to higher-BH-mass, more luminous AGNs. First, present-day observations do not have the spatial resolution needed to investigate regions of this size in such objects. Second, feeding $10^{8-9} M_\odot$ BHs in high-ionization AGNs by stellar winds would require a much larger stellar cluster and may involve different conditions. Direct mass inflow from the host likely plays the central role in such cases. Finally, we note recent results from Merloni et al. (2014) that compared the BH accretion rate and torus properties with total stellar mass and the SFR of the host galaxy. They indicate that the kiloparsec-scale stars and gas do not seem to have a direct causal connection with the BH and its immediate vicinity. A similar lack of correlation at low redshifts is shown in Koss et al. (2011).

7. UNIFICATION OR EVOLUTION?

7.1. Luminosity and Redshift Dependencies

As explained above, two categories of methods are used to estimate f_C . The first category includes all methods for measuring the covering factor of individual objects (see Section 3): the $L_{\text{dust}}/L_{\text{AGN}}$ method, the $\text{EW}(K_\alpha)$ method, and the method based on the scattered X-ray continuum. The $L_{\text{dust}}/L_{\text{AGN}}$ method results in the largest number of measured f_C . The second category includes methods that apply to the mean covering factor of the population. This is obtained by classifying a source as either a type-I or a type-II AGN and using the resulting $N_{\text{type-II,L}}/N_{\text{type-I,L}}$ ratio as an estimate of the mean value of f_C . One such method measures the X-ray-absorbing column and determines the AGN type relative to a fiducial absorbing column that separates the groups (e.g., Ueda et al. 2003, Gilli et al. 2007, Hasinger 2008, Brightman & Ueda 2012, Malizia et al. 2012). Another method counts the number of broad- and narrow-emission-line AGNs in optical and IR-selected samples. Ideally, all methods should agree but this is not the case (e.g., Lawrence &

Elvis 2010; Lusso et al. 2013, 2014; Mayo & Lawrence 2013). Mixed results are due to poorly understood physics of the torus, various selection effects, uncertainties in estimating L_{AGN} , and intrinsic reddening, among others. For example, the $L_{\text{dust}}/L_{\text{AGN}}$ method is based on dust emission from the torus and has little to do with BLR properties. However, X-ray absorption by gas in the BLR can increase the total measured X-ray column, thus decreasing L_{dust} because the ionizing radiation absorbed by the dust-free gas never interacts with the dusty torus. Here I focus on the large-sample approach, in particular on X-ray based studies.

The hard X-ray ($E > 2$ keV) spectrum of most AGNs can be described by a simple power law, $N_{pb} \propto E^{-\Gamma}$, where N_{pb} is the number of emitted photons per unit energy and time. A remarkable feature is the small scatter in the power-law slope, $\Gamma_{2-10 \text{ keV}} = 1.8 \pm 0.2$. This allows us to estimate the obscuring column density even in poor X-ray observations, provided we are looking through a single absorber. All that is required is a measure of the hardness ratio, e.g., $F(0.5-2 \text{ keV})/F(2-10 \text{ keV})$, and the redshift. The resulting accuracy in the measurement of the column is quite remarkable (~ 0.3 dex), with even higher accuracy in some cases of high photon flux that allow better modeling of the intrinsic continuum. The hydrogen column densities derived in this way range from thin (approximately 10^{21} cm^{-2}) to Compton thick ($> 1.25 \times 10^{24} \text{ cm}^{-2}$). Some of the results obtained thus far are hampered by selection effects. In particular, type-II sources are more likely to drop below the flux limit of the samples because of the increased absorption. This drop is less noticeable, but still present, in samples selected by their high energy flux (Malizia et al. 2012). The hardness ratio method can fail, sometimes dramatically, if the absorption is due to two or more LOS components, such as a combination of BLR clouds and a dusty torus gas (Section 4.2).

Merloni et al. (2014) provide a detailed study of X-ray obscuration. Their work is based on observations of the 2° XMM-COSMOS field and includes 1,310 sources of all types selected on the basis of their absorption-corrected 2–10 keV luminosity in the redshift range of 0.3–3.5. The rest-frame 2–10 keV flux limit is $2 \times 10^{-15} \text{ erg s}^{-1} \text{ cm}^{-2}$. The study supersedes earlier work of this type (e.g., Ueda et al. 2003, Gilli et al. 2007, Hasinger 2008, Malizia et al. 2012) that used data from other fields and instruments. It supplements a comprehensive study of type-I sources in the same field by Lusso et al. (2013). The spectral properties of the sources are described in Brusa et al. (2010) and Mainieri et al. (2011). The complete redshift information is based on spectroscopy and photometry and is of crucial importance because it allows researchers to use a simple K-correction and thus circumvent the well-known bias of flux-limited samples that tend to pick up more obscured sources at higher redshifts. A potential complication is a large number of Compton-thick sources that are unaccounted for. The number of these sources is still uncertain and depends on the survey, energy range used, and the spectroscopic analysis. It is generally estimated to be approximately 20% at low redshifts (Burlon et al. 2011) and approximately 40% at high redshifts (e.g., Brightman & Ueda 2012). In the COSMOS sample, which is not very deep, the numbers are smaller. There are also issues regarding the best way to correct the X-ray luminosity for absorption, in particular the simplistic way based only on hardness ratio with its well-known limitations.

An independent method that verifies the estimated numbers of obscured and unobscured AGNs is based on modeling the spectrum of the cosmic X-ray background (e.g., Comastri et al. 1995, Ueda et al. 2003). I do not go into the details of this method, which was reviewed and discussed in numerous papers (e.g., Gilli et al. 2007).

Can type-I and type-II sources classified by their optical properties be distinguished, unambiguously, by their X-ray-obscuring column? The answer is definitely no, although type-II sources are on average more obscured. Merloni et al. (2014) introduced a dividing column density of $N_H \simeq 10^{21.5} \text{ cm}^{-2}$ to separate the two types. They found that approximately 30% of optically classified type-I sources have obscuring columns larger than this value and that approximately

30% of optically classified type-II sources have obscuring columns smaller than this value. In fact, many, perhaps most, of the objects in these two groups may have little to do with obscuration by the torus. The sources in the latter group are the real type-II AGNs discussed above, and at least some of the objects in the first group are type-I AGNs with an X-ray source occulted by gas in the BLR or outflowing ionized gas in the opening of the torus. These two subgroups were not fully appreciated by the old unification scheme but are now known to influence the $N_{\text{type-I}}/N_{\text{type-II}}$ statistics.

Many of the real type-II AGNs in the local Universe are of very low luminosity and $L_{\text{AGN}}/L_{\text{Edd}}$ (Brightman & Nandra 2011b, Marinucci et al. 2012). Type-II AGNs in the XMM-COSMOS sample, at a redshift of approximately 0.3, are more luminous and can be considered intermediate-luminosity AGNs. An important clue to the nature of these sources is the presence or absence of a central obscurer. This can be tested by examining the $L(\text{MIR})/L(2\text{--}10\text{ keV})$ relationship discussed in Section 3. The real type-II objects in the Merloni et al. (2014) sample do not differ from other type-II AGNs in this respect. There is also direct evidence from *Spitzer* spectroscopy that the MIR SEDs of these sources are similar (but not identical) to the SEDs of type-II sources showing hidden broad emission lines (Tommasin et al. 2010). Many real type-II AGNs do not have enough high-density gas to result in a detectable BLR, but have central tori. This raises an interesting question about the relationship between the central source luminosity, the inner dimension of the torus, and the presence or absence of broad-emission-line gas. This question is discussed in Section 7.2.

Returning to the type-I sources with X-ray absorption, we note that for a Galactic dust-to-gas ratio, the above dividing column corresponds to $A_V \sim 1.7$ mag. If the obscurer is part of the dusty torus, then the intrinsic optical-UV spectrum of 30% of all type-I objects is expected to be heavily reddened. This is definitely not the case. As noted above, the obscuring gas may be part of the BLR, in which case it is dust-free. Alternatively, the absorbing gas is highly ionized, outflowing dust-free material (warm absorber, which is common in AGNs) (Turner & Miller 2009). The location of this gas may be well outside the BLR, including in the opening of the torus.

Figure 8 shows the fraction of obscured AGNs defined as a function of $L(2\text{--}10\text{ keV})$ by two different methods. Optical classification of AGNs shows a steep decrease in the fraction of obscured AGNs as a function of source luminosity, and X-ray classification shows a flat and weaker dependence on luminosity. Clearly, the large number of real type-II AGNs at low luminosity is the main reason for the difference between the two methods. This finding suggests a new, perhaps more intuitive definition of AGN types based only on the presence or absence of a central LOS obscurer. According to this classification, real type-II AGNs belong in the class of type-I AGNs (unobscured AGNs). In this case, the relative fraction of the two groups up to a redshift of about 1.5 is approximately 1:1 according to both the X-ray and optical methods.

The sample by Merloni et al. (2014) does not include low-redshift, very low-luminosity AGNs. A few notes about this end of the distribution are in order. First, the IR-selected sample of Brightman & Nandra (2011b) shows that the ratio $N_{\text{type-II}}/N_{\text{type-I}}$ peaks at approximately $L(2\text{--}10\text{ keV}) \sim 10^{42}\text{ erg s}^{-1}$ and drops to lower values below this luminosity. Second, the discrepancies illustrated in **Figure 8**, including those that are based on the measurements of individual covering factors (which are, occasionally, in poor agreement among themselves), are present in various other studies. A major discrepancy is, again, the confusion between host galaxy and torus obscuration, which is related to the large group of type-II sources.

What is the redshift evolution of obscured and unobscured AGNs? Observationally, this is challenging because of the small number of observed sources at high redshifts. Earlier works such as Hasinger (2008) claim the fraction of obscured sources increases with increasing redshift. This claim was questioned by Gilli et al. (2010) on grounds of a lack of an adequate K-correction.

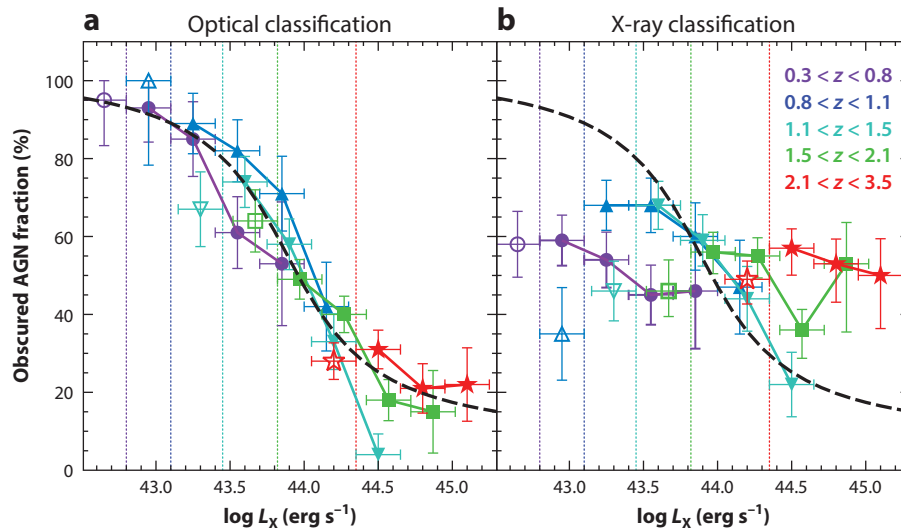


Figure 8

The fraction of obscured and unobscured AGNs at various redshifts and $L(2-10 \text{ keV})$. (a) Fractions obtained by optical classification. (b) Fractions obtained by a classification based on column densities derived from X-ray observations with a dividing column between the groups of $10^{21.5} \text{ cm}^{-2}$. Based on data from Merloni et al. (2014), courtesy of A. Merloni.

The study by Merloni et al. (2014), which is perhaps the most complete (a statement likely to be challenged by some X-ray astronomers), regarding low- and intermediate-luminosity sources is inconclusive. The results for the highest-luminosity AGNs are more significant, with indications for an increase in the fraction of obscured sources, with redshift amounting to a factor of approximately 2 between redshifts of 1 and 3. This finding is supported by several studies of AGNs in the *Chandra* Deep Field South (Brightman & Ueda 2012, Vito et al. 2013).

7.2. Receding and Approaching Tori and Disappearing BLRs

There have been several attempts to explain the dependence of the covering factor on source luminosity on the basis of the torus geometry. The idea of a receding torus, first suggested by Lawrence (1991), involves a simple torus whose height, h , is independent of the inner radius R_{in} . Because $R_{in} \propto L_{AGN}^{1/2}$, the covering factor is predicted to be proportional to $L_{AGN}^{-1/2}$. This ad hoc model makes no attempt to justify the constant height torus. It also does not explain the decreasing covering factors deduced from counting X-ray AGNs with different obscuring columns.

Extensive studies based on large samples of AGNs, some of which have already been mentioned, have tested the idea of a receding torus. None of these studies reproduced, accurately, the predicted dependence of f_C on L_{AGN} . There were several suggestions to modify the original idea. For example, Simpson (2005) measured the fraction of type-I sources by using [O III] $\lambda 5007$ luminosities in SDSS AGNs and constructing luminosity functions for the two types of AGNs. The author explained that the differences between the two luminosity functions were due to changes in the covering factor of the torus with luminosity and were claimed to be removed if $h \propto L_{AGN}^{0.23}$. Unfortunately, the work does not account for the conversion between $L([\text{O III}] \lambda 5007)$ and L_{AGN} , which is luminosity dependent (Stern & Laor 2012), a fact that was not known at the time. Ricci et al. (2013) used the observed EW(K_α) to suggest a somewhat different dependence.

These and other attempts are highly simplified and should not be viewed as more than simple analytic functions fitted to the observations. The increased inner radius with luminosity is indeed a solid and confirmed prediction of all torus models. However, other parameters, such as f_C and b , are not well defined and there is no simple theoretical reason to prefer a certain geometry over others. Finally, there are many observations showing that $L_{\text{dust}}/L_{\text{AGN}}$ is similar in very luminous AGNs and in sources that are 3–4 orders of magnitude less luminous. Such a luminosity difference corresponds to a factor ~ 100 in the distance between the torus inner walls and the BH, yet the torus geometry does not seem to be affected by much.

Researchers have used the idea of a luminosity-dependent sublimation radius to argue that below a certain L_{AGN} , the torus is likely to change its properties, even disappear. This idea deserves the name approaching tori. Several of its aspects were described in Laor (2003), Elitzur & Shlosman (2006), and Elitzur & Ho (2009). Laor (2003) suggested the sublimation radius as the outer boundary of the BLR be combined with the observed relationship between BH mass and L_{AGN} . This gives an estimate of the minimal broad-line velocity (taken here as the full width at half maximum, FWHM, of the broad $H\beta$ line), which is the Keplerian velocity at R_{in} . Using current RM results one finds

$$FWHM(H\beta) \simeq 1,700 M_8^{1/2} L_{46}^{-1/4} \text{ km s}^{-1}, \quad (7)$$

where, again, $L_{46} = L_{\text{AGN}}/10^{46} \text{ erg s}^{-1}$ and $M_8 = M_{\text{BH}}/10^8 M_{\odot}$. For $M_8 = 1$ and $L_{46} < 10^{-4}$, $FWHM(H\beta) > 17,000 \text{ km s}^{-1}$, a line width that is practically undetectable in low-luminosity AGNs whose continuum near the $H\beta$ line is dominated by stellar light. Additional considerations show that the line width may be related to $L_{\text{AGN}}/L_{\text{Edd}}$ rather than L_{AGN} . Laor (2003) further speculated that there is a natural limit to the maximum allowable velocity in the BLR and that clouds in this region close to the BH not only become undetectable but may not survive. Low-luminosity objects that appear to have only narrow high-ionization lines will be classified as real type-II AGNs and objects with low-ionization lines will be classified as type-II LINERs. This classification results in the increasing fraction of (apparent) type-II AGNs at low luminosities. The argument does not affect the covering factor of the torus. It applies mostly to extremely low-luminosity AGNs in the local Universe but not to the real type-II AGNs in the Merloni et al. (2014) sample where $L_{\text{AGN}} > 10^{43} \text{ erg s}^{-1}$.

Disappearing BLRs have been discussed by Nicastro (2000), who suggested that gas outflow from the surface of the disk, outside the region dominated by radiation pressure, can lead to disappearing BLRs at very low $L_{\text{AGN}}/L_{\text{Edd}}$. Elitzur & Ho (2009) followed the ideas developed in Elitzur & Shlosman (2006) and considered the clumpy dust-free BLR and the clumpy dusty torus as one entity made of clouds lifted along magnetic field lines from the surface of the disk. A limiting radial column density of approximately 10^{22} cm^{-2} was assumed to be a requirement for producing observable broad emission lines from the clumps. The work shows that at a low mass accretion rate, corresponding to $L_{\text{AGN}} \sim 10^{40}$, BLR clouds and large dusty clumps no longer exist. This luminosity, which varies with the BH mass and the corresponding $L_{\text{AGN}}/L_{\text{Edd}}$, is in the right ballpark for many LINERs but is several orders of magnitude smaller than the typical luminosity of many real type-II AGNs (Brightman & Nandra 2011b, Marinucci et al. 2012, Merloni et al. 2014). Despite the discrepancy, the general idea can perhaps be extended to include more luminous sources with no detectable broad emission lines.

7.3. Mergers, Evolution, and Unification

Detailed morphological studies reveal that about 80% of host galaxies of AGNs, up to a redshift of approximately 2, do not show signs of interaction (e.g., Cisternas et al. 2011, Schawinski et al.

2012). Such studies depend on the signal-to-noise ratio, spatial resolution, and most importantly redshift. They should be interpreted as strong evidence against major mergers and perhaps as weak evidence for the final stages of a minor merger where the mass ratio of the two hosts is large. The finding, which contradicts earlier claims about the association of most AGN activity with galaxy mergers, is evidence for the importance of secular processes in transporting cold gas from the disk to the vicinity of the BH. These studies show also that a large fraction of the most luminous AGNs at high redshifts are associated with mergers. Indeed, merger-induced nuclear activity is likely to be more common at high redshifts, when the density of the Universe was higher and much of the cold gas was not yet converted to stars. Can simple unification based on relatively simple shaped tori, and well-ordered motion of cold gas, be applied to the complex geometry of such mergers? How early in the history of a merger-triggered AGN can such an ordered central structure form? Can merger-driven AGNs be classified like the secularly evolving systems if their BLR is obscured by galactic scale dust (e.g., Imanishi et al. 2010)? What are the implications to the NIR–MIR SEDs of such systems?

Major mergers of gas-rich systems in the early Universe have been suggested to result in powerful dusty SF systems (dust-obscured galaxies, DOGs) surrounding a buried AGN whose power increases with time (see Narayanan et al. 2010 and references therein). As the power of the AGN increases, the surrounding gas is blown away and an unobscured AGN is revealed. The most luminous AGNs during the era of peak AGN activity, at $z = 2\text{--}3$ AGNs, have been suggested to be this type of object. In this case the geometry of the obscuring dust must be different from the geometry of simple tori assumed in nonmerging galaxies. Unfortunately, numerical merger simulations do not yet have sufficient resolution to model the geometry of such structures and high-resolution imaging is limited to nearby systems (see, however, Schawinski et al. 2012). Thus, SED observations and model fitting are the best tools to investigate these scenarios, particularly in objects for which both optical and IR information are available (e.g., SDSS and WISE; see Weedman et al. 2012, Vardanyan et al. 2014).

An empirical way to study such scenarios is to examine objects with very large $L_{\text{dust}}/L_{\text{AGN}}$ ratios and check whether this is caused by UV luminosity, which is unusually low (UV extinction in a DOG), or MIR luminosity, which is unusually high (large covering factor and a clear LOS to the center). Vardanyan et al. (2014) suggest that the latter is correct and show that the objects with the smallest $L_{\text{dust}}/L_{\text{AGN}}$ ratio are those with the largest $L(\text{UV})$. Such studies show no evidence of the DOG-related scenario for $z = 2\text{--}3$ AGNs [see, however, Glikman et al. (2012) for evidence to the contrary].

There are more detailed studies of merging systems at low and intermediate redshifts, especially ultraluminous infrared galaxies (ULIRGs) hosting active BHs. A low-redshift sample of this type is the QUEST (Quasar/ULIRG Evolutionary Study) sample (see Veilleux et al. 2006, 2009a,b, and references therein). Some of the sources in the QUEST sample contain low-luminosity AGNs, including LINERs, and are clearly SF-dominated systems. Other sources contain high-luminosity AGNs, mostly Palomar–Green quasars. HST imaging of QUEST sources indicate that AGN type depends on the evolutionary stage of the host, and the BH activity is triggered most likely by the merger. In particular, there is evidence that a merger progresses from type-II at the earlier stages to type-I near its final stage. Type-I AGNs become more common among fully coalesced merger remnants with ellipse-like hosts (Veilleux et al. 2006). They also become more common with increasing L_{dust} . This may or may not be related to the general trend of decreasing obscuration with increasing $L(2\text{--}10\text{ keV})$ discussed for nonmerging systems. Many of the QUEST sources have been observed, spectroscopically, by *Spitzer*. Comparisons of QUEST sources with sources that show no indication of mergers (Mor et al. 2009, Mor & Netzer 2012) show similar SEDs and a similar trend of decreasing covering factor with increasing L_{AGN} .

Can major mergers at high redshifts produce galactic scale obscuration that results in torus-like SED and absorption? Can heating by the AGN result in cold (30–50 K) dust emission that mimics SF regions? There are no clear observational answers to these questions, but recent calculations by Schneider et al. (2014) give some clues.

A complex geometry that can give rise to both MIR and FIR (far-infrared) emission is a torus within a torus or an obscurer within an obscurer. In this scenario, a large-covering-factor obscurer, just outside the dust sublimation radius, results in intense NIR–MIR emission. This obscurer is clumpy and has a simple axisymmetric geometry. Part of the AGN radiation escapes through its ionization cones and part of it leaks through the clumps. A much larger obscurer, with an undefined geometry that does not block the central dust-free cone, is present at a distance of a few kiloparsecs. The covering factor of the inner obscurer is f_c (in) and the covering factor of the outer obscurer f_c (out). It is easy to think of several scenarios that result in different relative $L(\text{FIR})/L(\text{MIR})/L_{\text{AGN}}$ ratios, depending on how much radiation from the central source leaks through the small obscurer near the center. Some of the NIR–MIR radiation of the central obscurer might be absorbed by the farther dust if its optical depth is large enough. A certain variant of this complex geometry was modeled by Schneider et al. (2014), who found that such a geometry, with f_c (in) in the range of 0.5–0.7, gives a reasonable fit to the observed SED of a specific $z = 6.4$ AGNs. In that particular model, approximately half of the FIR luminosity is AGN related and half is SF related.

An obvious observational test would be to obtain polarimetry maps of such systems, since this is a most effective way to check whether the distribution of the position angles is centrosymmetric (i.e., scattering from a central point) (see Kishimoto 1999).

In summary, it is hard to imagine that major mergers, especially in the early Universe, can lead to the highly ordered geometry, and the torus-like structure, suggested to explain the observations of lower-luminosity, secularly evolving systems. Detailed SED studies of high-redshift mergers can help resolve this issue.

SUMMARY: PRESENT AND FUTURE UNIFICATION

The unification scheme presented in this review is different from and similar to the scheme presented in the late 1980s, which had three fundamental pillars: orientation, covering factor, and luminosity. The field is driven by courageous attempts to construct simple models for complex situations, and attempts to understand several selection effects typical of large samples. The most important developments of the last decade or so are summarized as follows.

1. Most AGN tori are probably axisymmetric and clumpy. Unfortunately, today’s phenomenological clumpy torus models leave much to be desired and their parameters are hard to constrain. Hydrodynamic calculations that follow the inflow of gas from the galaxy are more promising. AGN tori naturally produce a clumpy thick central structure and demonstrate the importance of SN explosions and radiation pressure feedback by the central AGN. The simulations do not yet include all relevant processes and are generally limited to AGNs with small BHs.
2. Disk wind models of different types seem to explain several fundamental properties of the central obscurer, such as the formation of dust-free and dusty clumps at roughly the desired locations. So far, there is no clear preference for magnetic or radiation-pressure-driven winds, and for all models, forming and maintaining large-column-density clumps remains problematic.
3. The central issues of the covering factor and anisotropy of the torus are not yet fully understood. The general trend of decreasing f_c with increasing L_{AGN} is seen in some but not all studies and its details are not well understood. There are substantial disagreements

between the various methods used to study this relationship, such as the methods based on the $L_{\text{dust}}/L_{\text{AGN}}$ ratio, on $\text{EW}(\text{K}\alpha)$, or on dividing the population into groups on the basis of X-ray-absorbing columns. The suggestion of a receding torus is the only theoretical idea driving this field. However, the idea is neither physically sound nor well understood.

4. The mapping of central ionization cones and IR interferometry have led to major developments in this field. Bicone observations provide the most reliable way to define the torus boundaries and link the emission-line properties to the kinematic properties of the NLR gas. Long-baseline interferometry is the wave of the future. It has already provided global intriguing results, such as an unexpected run of dust temperature, with radius and model images that indicate deviations from a simple torus-shaped obscurer. The IR interferometry also stresses the need to reconsider the role of MIR-emitting polar outflows. Phase information in the future will likely provide real images of central AGN tori.
5. Part of the confusion in the present unification scheme results from the presence of several subgroups that may not belong in it in the first place. In particular, real type-II AGNs, which are not really understood, confuse several issues such as the fraction of obscured and unobscured low-luminosity AGNs. Another group that shows an assortment of properties is type-Ii AGNs. Some type-Ii AGNs are heavily extinguished by dust in the host galaxy; others are type-I AGNs caught during a time of minimum AGN activity.
6. Unification does not seem to stand the test of BH evolution. In particular, merging systems likely behave in a way different from that of AGNs in secularly evolving hosts. On the basis of today's observations, there is no reason to believe that accreting BHs in major mergers, or merger remnants, partake in the simple, old unification scheme.

Returning to the central theme of unification, it is clear that the old scheme requires several major revisions. More important revisions include the recognition that there is a large range of covering factors for a given luminosity, the realization that X-ray absorption can be caused by two or possibly more components, and the identification of several subgroups of AGNs that do not belong in this scheme in the first place. A revised scheme would require better methods to isolate and remove cases in which obscuration has nothing to do with the nucleus, and improved X-ray techniques to clarify the importance of X-ray absorption by dust-free gas. Perhaps the most crucial aspect, which is observationally challenging, is the separation of torus absorption from the presence of broad emission lines. Putting the absorption of the nonstellar continuum in the center of the scheme and minimizing the use of broad emission lines as a major characteristics are good ways to proceed.

DISCLOSURE STATEMENT

The author is not aware of any affiliations, memberships, funding, or financial holdings that might be perceived as affecting the objectivity of this review.

ACKNOWLEDGMENTS

This review benefitted from comments and suggestions by colleagues and friends who shared with me their broad knowledge and deep understanding of this field. Special thanks go to Ski Antonucci, Murray Brightman, Leonard Bartscher, Mike Crenshaw, Ric Davies, Michael Dopita, Moshe Elitzur, Martin Elvis, Jacopo Fritz, Josefa Masegosa Gallego, Sebastian Hönig, Steven Kraemer, Ari Laor, Andy Lawrence, Dieter Lutz, Vincenzo Mainieri, Roberto Maiolino, Andrea Merloni, Richard Mushotzky, Cristina Ramos-Almeida, Guido Risaliti, David Rosario, Mara Salvato, Marc

Schartmann, Allan Schnorr Müller, Marko Stalevski, Clive Tadhunter, Konrad Tristram, Jane Turner, Sylvain Veilleux, Keiichi Wada, and Belinda Wilkes.

LITERATURE CITED

- Aalto S, Garcia-Burillo S, Muller S, et al. 2015. *Astron. Astrophys.* 574:A85
- Alexander T, Lutz D, Sturm E, et al. 2000. *Ap. J.* 536:710–17
- Alig C, Schartmann M, Burkert A, Dolag K. 2013. *Ap. J.* 771:119
- Alonso-Herrero A, Ramos Almeida C, Mason R, et al. 2011. *Ap. J.* 736:82
- Antonucci R. 1993. *Annu. Rev. Astron. Astrophys.* 31:473–521
- Antonucci RRJ, Miller JS. 1985. *Ap. J.* 297:621–32
- Asmus D, Gandhi P, Smette A, Hönig SF, Duschl WJ. 2011. *Astron. Astrophys.* 536:A36
- Assef RJ, Stern D, Kochanek CS, et al. 2013. *Ap. J.* 772:26
- Baldwin JA, Phillips MM, Terlevich R. 1981. *Publ. Astron. Soc. Pac.* 93:5–19
- Barvainis R. 1987. *Ap. J.* 320:537
- Beckert T, Duschl WJ. 2004. *Astron. Astrophys.* 426:445–54
- Bentz MC, Denney KD, Grier CJ, et al. 2013. *Ap. J.* 767:149
- Bianchi S, Bonilla NF, Guainazzi M, Matt G, Ponti G. 2009. *Astron. Astrophys.* 501:915
- Bianchi S, Guainazzi M, Chiaberge M. 2006. *Astron. Astrophys.* 448:499–511
- Blandford RD, Netzer H, Woltjer L, Courvoisier TJL, Mayor M, eds. 1990. *Active Galactic Nuclei*. Heidelberg, Ger.: Springer-Verlag
- Bock JJ, Neugebauer G, Matthews K, et al. 2000. *Astron. J.* 120:2904–19
- Bottorff MC, Korista KT, Shlosman I. 2000. *Ap. J.* 537:134–51
- Brightman M, Nandra K. 2011a. *MNRAS* 413:1206–35
- Brightman M, Nandra K. 2011b. *MNRAS* 414:3084–104
- Brightman M, Ueda Y. 2012. *MNRAS* 423:702–17
- Brusa M, Civano F, Comastri A, et al. 2010. *Ap. J.* 716:348–69
- Buchanan CL, Gallimore JF, O’Dea CP, et al. 2006. *Astron. J.* 132:401–19
- Burlon D, Ajello M, Greiner J, et al. 2011. *Ap. J.* 728:58
- Burtscher L, Meisenheimer K, Tristram KRW, et al. 2013. *Astron. Astrophys.* 558:A149
- Caproni A, Livio M, Abraham Z, Mosquera Cuesta HJ. 2006. *Ap. J.* 653:112–26
- Chaudhary P, Brusa M, Hasinger G, Merloni A, Comastri A. 2010. *Astron. Astrophys.* 518:A58
- Cid Fernandes R, Stasińska G, Mateus A, Vale Asari N. 2011. *MNRAS* 413:1687–99
- Cisternas M, Jahnke K, Bongiorno A, et al. 2011. *Ap. J. Lett.* 741:L11
- Collin S, Zahn JP. 1999. *Astron. Astrophys.* 344:433–49
- Collin S, Zahn JP. 2008. *Astron. Astrophys.* 477:419–35
- Comastri A, Setti G, Zamorani G, Hasinger G. 1995. *Astron. Astrophys.* 296:1
- Combes F, García-Burillo S, Casasola V, et al. 2013. *Astron. Astrophys.* 558:A124
- Czerny B, Hryniewicz K. 2011. *Astron. Astrophys.* 525:L8
- Davies R, Mark D, Sternberg A. 2012. *Astron. Astrophys.* 537:A133
- Davies RI, Maciejewski W, Hicks EKS, et al. 2014. *Ap. J.* 792:101
- Davies RI, Müller-Sánchez F, Genzel R, et al. 2007. *Ap. J.* 671:1388–412
- Deo RP, Crenshaw DM, Kraemer SB, et al. 2007. *Ap. J.* 671:124–35
- Deo RP, Richards GT, Crenshaw DM, Kraemer SB. 2009. *Ap. J.* 705:14–31
- Diamond-Stanic AM, Rieke GH. 2012. *Ap. J.* 746:168
- Diamond-Stanic AM, Rieke GH, Rigby JR. 2009. *Ap. J.* 698:623–31
- Díaz-Santos T, Alonso-Herrero A, Colina L, et al. 2010. *Ap. J.* 711:328–49
- Dicken D, Tadhunter C, Morganti R, et al. 2014. *Ap. J.* 788:98
- Dopita MA, Scharwächter J, Shastri P, et al. 2014. *Astron. Astrophys.* 566:A41
- Dullemond CP, van Bemmell IM. 2005. *Astron. Astrophys.* 436:47–56
- Duschl WJ, Britsch M. 2006. *Ap. J. Lett.* 653:L89–92
- Efstathiou A, Rowan-Robinson M. 1995. *MNRAS* 273:649–61

- Elitzur M. 2012. *Ap. J. Lett.* 747:L33
- Elitzur M, Ho LC. 2009. *Ap. J. Lett.* 701:L91–94
- Elitzur M, Shlosman I. 2006. *Ap. J. Lett.* 648:L101–4
- Elvis M. 2012. *J. Phys. Conf. Ser.* 372:012032
- Emmering RT, Blandford RD, Shlosman I. 1992. *Ap. J.* 385:460–77
- Esquej P, Alonso-Herrero A, González-Martín O, et al. 2014. *Ap. J.* 780:86
- Feltre A, Hatziminaoglou E, Fritz J, Franceschini A. 2012. *MNRAS* 426:120–27
- Fischer TC, Crenshaw DM, Kraemer SB, Schmitt HR. 2013. *Ap. J. Suppl.* 209:1
- Fischer TC, Crenshaw DM, Kraemer SB, Schmitt HR, Turner TJ. 2014. *Ap. J.* 785:25
- Fritz J, Franceschini A, Hatziminaoglou E. 2006. *MNRAS* 366:767–86
- Gandhi P, Horst H, Smette A, et al. 2009. *Astron. Astrophys.* 502:457
- García-Burillo S, Combes F, Usero A, et al. 2014. *Astron. Astrophys.* 567:A125
- Gilli R, Comastri A, Hasinger G. 2007. *Astron. Astrophys.* 463:79–96
- Gilli R, Comastri A, Vignali C, Ranalli P, Iwasawa K. 2010. In *X-ray Astronomy 2009; Present Status, Multi-Wavelength Approach and Future Perspectives*, ed. A Comastri, L Angelini, M Cappi. *AIP Conf. Proc.* 1248:359–64. Melville, NY: AIP
- Glass IS. 1992. *MNRAS* 256:P23–27
- Glikman E, Gregg MD, Lacy M, et al. 2004. *Ap. J.* 607:60–75
- Glikman E, Urrutia T, Lacy M, et al. 2012. *Ap. J.* 757:51
- González-Martín O, Rodríguez-Espinosa JM, Díaz-Santos T, et al. 2013. *Astron. Astrophys.* 553:A35
- Goulding AD, Alexander DM. 2009. *MNRAS* 398:1165–93
- Goulding AD, Alexander DM, Bauer FE, et al. 2012. *Ap. J.* 755:5
- Granato GL, Danese L, Franceschini A. 1997. *Ap. J.* 486:147–59
- Greenhill LJ, Booth RS, Ellingsen SP, et al. 2003. *Ap. J.* 590:162–73
- Haas M, Willner SP, Heymann F, et al. 2008. *Ap. J.* 688:122–27
- Hailey-Dunsheath S, Sturm E, Fischer J, et al. 2012. *Ap. J.* 755:57
- Hasinger G. 2008. *Astron. Astrophys.* 490:905–22
- Heckman T, Best P. 2014. *Annu. Rev. Astron. Astrophys.* 52:589
- Hernández-García L, González-Martín O, Márquez I, Masegosa J. 2013. *Astron. Astrophys.* 556:A47
- Hicks EKS, Davies RI, Malkan MA, et al. 2009. *Ap. J.* 696:448–70
- Ho LC. 2008. *Annu. Rev. Astron. Astrophys.* 46:475–539
- Hönig SF, Beckert T. 2007. *MNRAS* 380:1172–76
- Hönig SF, Kishimoto M, Gandhi P, et al. 2010. *Astron. Astrophys.* 515:A23
- Hönig SF, Kishimoto M, Tristram KRW, et al. 2013. *Ap. J.* 771:87
- Hönig SF, Leipski C, Antonucci R, Haas M. 2011. *Ap. J.* 736:26
- Ikeda S, Awaki H, Terashima Y. 2009. *Ap. J.* 692:608–17
- Imanishi M, Maiolino R, Nakagawa T. 2010. *Ap. J.* 709:801–15
- Iwasawa K, Taniguchi Y. 1993. *Ap. J. Lett.* 413:L15–18
- Jaffe W, Meisenheimer K, Röttgering HJA, et al. 2004. *Nature* 429:47–49
- Kartje JF, Königl A. 1996. *Vistas Astron.* 40:133–37
- Kaspi S, Smith PS, Netzer H, et al. 2000. *Ap. J.* 533:631–49
- Kauffmann G, Heckman TM, Tremonti C, et al. 2003. *MNRAS* 346:1055–77
- Kawaguchi T, Mori M. 2010. *Ap. J. Lett.* 724:L183
- Kawaguchi T, Mori M. 2011. *Ap. J.* 737:105
- Kewley LJ, Groves B, Kauffmann G, Heckman T. 2006. *MNRAS* 372:961–76
- Kinkhabwala A, Sako M, Behar E, et al. 2002. *Ap. J.* 575:732–46
- Kinney AL, Schmitt HR, Clarke CJ, et al. 2000. *Ap. J.* 537:152–77
- Kishimoto M. 1999. *Ap. J.* 518:676–92
- Kishimoto M, Hönig SF, Antonucci R, et al. 2011a. *Astron. Astrophys.* 527:A121
- Kishimoto M, Hönig SF, Antonucci R, et al. 2011b. *Astron. Astrophys.* 536:A78
- Kishimoto M, Hönig SF, Beckert T, Weigelt G. 2007. *Astron. Astrophys.* 476:713–21
- Königl A, Kartje JF. 1994. *Ap. J.* 434:446–67
- Koshida S, Minezaki T, Yoshii Y, et al. 2014. *Ap. J.* 788:159

- Koss M, Mushotzky R, Veilleux S, et al. 2011. *Ap. J.* 739:57
- Kraemer SB, Schmitt HR, Crenshaw DM. 2008. *Ap. J.* 679:1128–43
- Kraemer SB, Schmitt HR, Crenshaw DM, et al. 2011. *Ap. J.* 727:130
- Kreimeyer K, Veilleux S. 2013. *Ap. J. Lett.* 772:L11
- Krips M, Martin S, Eckart A, et al. 2011. *Ap. J.* 736:37
- Krolik JH. 1998. *Active Galactic Nuclei: From the Central Black Hole to the Galactic Environment*. Princeton, NJ: Princeton Univ. Press
- Krolik JH. 2007. *Ap. J.* 661:52–59
- Krolik JH, Begelman MC. 1988. *Ap. J.* 329:702
- Lacy M, Petric AO, Sajina A, et al. 2007. *Astron. J.* 133:186–205
- Lagos CDP, Padilla ND, Strauss MA, Cora SA, Hao L. 2011. *MNRAS* 414:2148–62
- LaMassa SM, Heckman TM, Ptak A, et al. 2011. *Ap. J.* 729:52
- Laor A. 2003. *Ap. J.* 590:86–94
- Laor A, Netzer H. 1989. *MNRAS* 238:897–916
- Lawrence A. 1991. *R. Astron. Soc.* 252:586–92
- Lawrence A, Elvis M. 1982. *Ap. J.* 256:410–26
- Lawrence A, Elvis M. 2010. *Ap. J.* 714:561–70
- Leipski C, Haas M, Willner SP, et al. 2010. *Ap. J.* 717:766–75
- Levenson NA, Radomski JT, Packham C, et al. 2009. *Ap. J.* 703:390–98
- Lira P, Videla L, Wu Y, et al. 2013. *Ap. J.* 764:159
- Lusso E, Hennawi JF, Comastri A, et al. 2013. *Ap. J.* 777:86
- Lusso E, Hennawi JF, Comastri A, et al. 2014. *Ap. J.* 784:176
- Lutz D, Maiolino R, Moorwood AFM, et al. 2002. *Astron. Astrophys.* 396:439–48
- Lutz D, Maiolino R, Spoon HWW, Moorwood AFM. 2004. *Astron. Astrophys.* 418:465–73
- Mainieri V, Bongiorno A, Merloni A, et al. 2011. *Astron. Astrophys.* 535:A80
- Maiolino R. 2008. *New Astron. Rev.* 52:339–57
- Maiolino R, Marconi A, Salvati M, et al. 2001. *Astron. Astrophys.* 365:28–36
- Maiolino R, Risaliti G, Salvati M, et al. 2010. *Astron. Astrophys.* 517:A47
- Maiolino R, Shemmer O, Imanishi M, et al. 2007. *Astron. Astrophys.* 468:979–92
- Malizia A, Bassani L, Bazzano A, et al. 2012. *MNRAS* 426:1750–66
- Malkan MA, Gorjian V, Tam R. 1998. *Ap. J. Suppl.* 117:25–88
- Maoz D. 2007. *MNRAS* 377:1696–710
- Marinucci A, Bianchi S, Nicastro F, Matt G, Goulding AD. 2012. *Ap. J.* 748:130
- Markowitz AG, Krumpe M, Nikutta R. 2014. *MNRAS* 439:1403–58
- Mayo JH, Lawrence A. 2013. *MNRAS* 434:1593–98
- Merloni A, Bongiorno A, Brusa M, et al. 2014. *MNRAS* 437:3550–67
- Merloni A, Heinz S. 2013. In *Planets, Stars and Stellar Systems*, ed. TD Oswalt, WC Keel, 6:503–66. Dordrecht, Neth.: Springer
- Meusinger H, Balafkan N. 2014. *Astron. Astrophys.* 568:A114
- Mor R, Netzer H. 2012. *MNRAS* 420:526–41
- Mor R, Netzer H, Elitzur M. 2009. *Ap. J.* 705:298–313
- Mor R, Trakhtenbrot B. 2011. *Ap. J. Lett.* 737:L36
- Mulchaey JS, Wilson AS, Tsvetanov Z. 1996. *Ap. J.* 467:197
- Mullaney JR, Alexander DM, Goulding AD, Hickox RC. 2011. *MNRAS* 414:1082–110
- Müller-Sánchez F, Prieto MA, Hicks EKS, et al. 2011. *Ap. J.* 739:69
- Narayan R. 2005. *Ap. Space Sci.* 300:177
- Narayanan D, Dey A, Hayward CC, et al. 2010. *MNRAS* 407:1701–20
- Nenkova M, Sirocky MM, Ivezić V, Elitzur M. 2008a. *Ap. J.* 685:147–59
- Nenkova M, Sirocky MM, Nikutta R, Ivezić V, Elitzur M. 2008b. *Ap. J.* 685:160–80
- Netzer H. 1993. *Ap. J.* 411:594–601
- Netzer H. 2009. *MNRAS* 399:1907–20
- Netzer H. 2013. *The Physics and Evolution of Active Galactic Nuclei*. Cambridge, UK: Cambridge Univ. Press
- Netzer H, Laor A. 1993. *Ap. J. Lett.* 404:L51–54

- Netzer H, Trakhtenbrot B. 2014. *MNRAS* 438:672–79
- Nicastro F. 2000. *Ap. J. Lett.* 530:L65–68
- Ogle PM, Marshall HL, Lee JC, Canizares CR. 2000. *Ap. J. Lett.* 545:L81–84
- Osterbrock DE, Ferland GJ. 2006. *Astrophysics of Gaseous Nebulae and Active Galactic Nuclei*. Sausalito, CA: Univ. Sci. Books. 2nd ed.
- Paggi A, Wang J, Fabbiano G, Elvis M, Karovska M. 2012. *Ap. J.* 756:39
- Panessa F, Bassani L. 2002. *Astron. Astrophys.* 394:435–42
- Peeters E, Spoon HWW, Tielens AGGM. 2004. *Ap. J.* 613:986–1003
- Peterson BM. 1997. *An Introduction to Active Galactic Nuclei*. Cambridge, UK: Cambridge Univ. Press
- Pier EA, Krolik JH. 1992. *Ap. J.* 401:99
- Pogge RW. 1988. *Ap. J.* 328:519–22
- Pott JU, Malkan MA, Elitzur M, et al. 2010. *Ap. J.* 715:736–42
- Pozo Nuñez F, Haas M, Chini R, et al. 2014. *Astron. Astrophys.* 561:L8
- Prieto MA, Mezcua M, Fernández-Ontiveros JA, Schartmann M. 2014. *MNRAS* 442:2145–64
- Ramos Almeida C, Alonso-Herrero A, Levenson NA, et al. 2014. *MNRAS* 439:3847–59
- Ramos Almeida C, Levenson NA, Alonso-Herrero A, et al. 2011. *Ap. J.* 731:92
- Reyes R, Zakamska NL, Strauss MA, et al. 2008. *Astron. J.* 136:2373–90
- Ricci C, Paltani S, Awaki H, et al. 2013. *Astron. Astrophys.* 553:A29
- Rieke GH, Alonso-Herrero A, Weiner BJ, et al. 2009. *Ap. J.* 692:556–73
- Riffel R, Riffel RA, Ferrari F, Storchi-Bergmann T. 2011. *MNRAS* 416:493–500
- Riffel RA, Storchi-Bergmann T, Riffel R, Pastoriza MG. 2010. *Ap. J.* 713:469–74
- Riffel RA, Storchi-Bergmann T, Winge C. 2013. *MNRAS* 430:2249–61
- Risaliti G, Elvis M, Fabbiano G, et al. 2007. *Ap. J. Lett.* 659:L111–14
- Risaliti G, Elvis M, Nicastro F. 2002. *Ap. J.* 571:234–46
- Risaliti G, Nardini E, Salvati M, et al. 2011. *MNRAS* 410:1027–35
- Robson IEI. 1996. *Active Galactic Nuclei*. New York: Wiley
- Rosario DJ, Santini P, Lutz D, et al. 2013. *Ap. J.* 771:63
- Rosario DJ, Santini P, Lutz D, et al. 2012. *Astron. Astrophys.* 545:A45
- Roseboom IG, Lawrence A, Elvis M, et al. 2013. *MNRAS* 429:1494–501
- Sako M, Kahn SM, Paerels F, Liedahl DA. 2000. *Ap. J. Lett.* 543:L115–18
- Schartmann M, Burkert A, Krause M, et al. 2010. *MNRAS* 403:1801–11
- Schartmann M, Meisenheimer K, Camenzind M, et al. 2008. *Astron. Astrophys.* 482:67–80
- Schartmann M, Meisenheimer K, Camenzind M, Wolf S, Henning T. 2005. *Astron. Astrophys.* 437:861–81
- Schawinski K, Simmons BD, Urry CM, Treister E, Glikman E. 2012. *MNRAS* 425:L61–65
- Schneider R, Bianchi S, Valiante R, Risaliti G, Salvadori S. 2014. arXiv:1402.2279
- Schnorr-Müller A, Storchi-Bergmann T, Nagar NM, et al. 2014. *MNRAS* 437:1708–24
- Schweitzer M, Groves B, Netzer H, et al. 2008. *Ap. J.* 679:101–17
- Shemmer O, Trakhtenbrot B, Anderson SF, et al. 2010. *Ap. J. Lett.* 722:L152–56
- Shi Y, Rieke GH, Smith P, et al. 2010. *Ap. J.* 714:115–29
- Simpson C. 2005. *MNRAS* 360:565–72
- Stalevski M, Fritz J, Baes M, Nakos T, Popović LC. 2012. *MNRAS* 420:2756–72
- Stern D, Eisenhardt P, Gorjian V, et al. 2005. *Ap. J.* 631:163–68
- Stern J, Laor A. 2012. *MNRAS* 426:2703–18
- Storchi-Bergmann T, Riffel RA, Riffel R, et al. 2012. *Ap. J.* 755:87
- Suganuma M, Yoshii Y, Kobayashi Y, et al. 2006. *Ap. J.* 639:46–63
- Swain M, Vasisht G, Akeson R, et al. 2003. *Ap. J. Lett.* 596:L163–66
- Tadhunter C. 2008. *New Astron. Rev.* 52:227–39
- Tadhunter C, Tsvetanov Z. 1989. *Nature* 341:422–24
- Tommasin S, Spinoglio L, Malkan MA, Fazio G. 2010. *Ap. J.* 709:1257–83
- Torricelli-Ciamponi G, Pietrini P, Risaliti G, Salvati M. 2014. *MNRAS* 442:2116–30
- Tran HD. 2003. *Ap. J.* 583:632–48
- Treister E, Krolik JH, Dullemond C. 2008. *Ap. J.* 679:140–48
- Tristram KRW, Burtscher L, Jaffe W, et al. 2014. *Astron. Astrophys.* 563:A82

- Trump JR, Impey CD, Taniguchi Y, et al. 2009. *Ap. J.* 706:797–809
- Turner TJ, Miller L. 2009. *Astron. Astrophys. Rev.* 17:47–104
- Ueda Y, Akiyama M, Ohta K, Miyaji T. 2003. *Ap. J.* 598:886–908
- Ueda Y, Eguchi S, Terashima Y, et al. 2007. *Ap. J. Lett.* 664:L79–82
- Urry CM, Padovani P. 1995. *Publ. Astron. Soc. Pac.* 107:803
- Urry M. 2003. In *Active Galactic Nuclei: From Central Engine to Host Galaxy*, ed. S Collin, F Combes, I Shlosman. *ASP Conf. Ser.* 290:3. San Francisco: ASP
- Vardanyan V, Weedman D, Sargsyan L. 2014. *Ap. J.* 790:88
- Veilleux S, Kim DC, Peng CY, et al. 2006. *Ap. J.* 643:707–23
- Veilleux S, Kim DC, Rupke DSN, et al. 2009a. *Ap. J.* 701:587–606
- Veilleux S, Osterbrock DE. 1987. *Ap. J. Suppl.* 63:295–310
- Veilleux S, Rupke DSN, Kim DC, et al. 2009b. *Ap. J. Suppl. Ser.* 182:628–66
- Vito F, Vignali C, Gilli R, et al. 2013. *MNRAS* 428:354–69
- Vollmer B, Beckert T, Davies RI. 2008. *Astron. Astrophys.* 491:441–53
- Wada K. 2012. *Ap. J.* 758:66
- Wada K, Papadopoulos PP, Spaans M. 2009. *Ap. J.* 702:63–74
- Wang J, Fabbiano G, Elvis M, et al. 2011a. *Ap. J.* 742:23
- Wang JM, Ge JQ, Hu C, et al. 2011b. *Ap. J.* 739:3
- Wang JM, Qiu J, Du P, Ho LC. 2014. *Ap. J.* 797:65
- Wang JM, Yan CS, Gao HQ, et al. 2010. *Ap. J. Lett.* 719:L148–52
- Weaver KA, Meléndez M, Mushotzky RF, et al. 2010. *Ap. J.* 716:1151–65
- Weedman D, Sargsyan L, Lebouteiller V, Houck J, Barry D. 2012. *Ap. J.* 761:184
- Weigelt G, Hofmann KH, Kishimoto M, et al. 2012. *Astron. Astrophys.* 541:L9
- Yaqoob T, Murphy KD, Miller L, Turner TJ. 2010. *MNRAS* 401:411–17